

**GLOBAL OPTIMISATION APPROACH FOR MAGNETIC
AND IP/RESISTIVITY DATA TO DECIPHER
SUBSURFACE STRUCTURAL FEATURES AND
CONDUCTIVE ZONES FAVOURABLE FOR URANIUM
MINERALISATION IN RAJPURA AREA, NE OF
PRITHIVIPURA, SIKAR DISTRICT, RAJASTHAN**

by

BIBHU PRASAD DAS

ENGG1G201801003

Bhabha Atomic Research Centre, Mumbai

*A thesis submitted to the
Board of Studies in Engineering Sciences*

In partial fulfillment of requirements

for the Degree of

MASTER OF TECHNOLOGY

of

HOMI BHABHA NATIONAL INSTITUTE

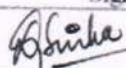
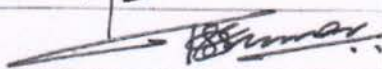

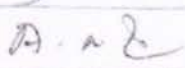
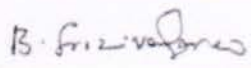


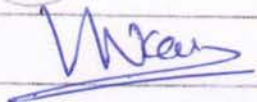


February, 2021

Homi Bhabha National Institute

Recommendations of the Thesis Examining Committee

As members of the Thesis examining Committee, we recommend that the thesis prepared by Bibhu Prasad Das entitled "Global optimisation approach for magnetic and IP/Resistivity data to decipher subsurface structural features and conductive zones favourable for uranium mineralisation in Rajpura area, NE of Prithvipura, Sikar district, Rajasthan" be accepted as fulfilling the thesis requirement for the Degree of Master of Technology.

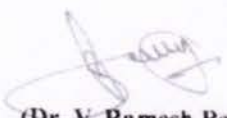
	Name	Signature
Member-1	Dr. D. K. Sinha	
Member-2	Dr. T. S. Sunil Kumar	
Member-3	Dr. V. Ramesh Babu	
Member-4	Dr. A. Rama Raju	
Technical advisor	B. Srinivasa Rao	
Examiner	Dr. K. Naganjaneyulu	
Guide & Convener	Dr. V. Ramesh Babu	
Chairman	Prof. Vivekanand Kain	

Final approval and acceptance of this thesis is contingent upon the candidate's submission of the final copies of the thesis to HBNI.

I hereby certify that I have read this thesis prepared under my direction and recommend that it may be accepted as fulfilling the thesis requirement.

Date: 11-02-2021

Place: Hyderabad


(Dr. V. Ramesh Babu)
Guide

DECLARATION

I, hereby, declare that the investigations presented in the thesis have been carried out by me. The work is original and has not been submitted earlier as a whole or in part for a degree/diploma at this or any other Institution / University.

Bibhu Prasad Das

(Bibhu Prasad Das)

CONTENTS

Synopsis	V
List of figures	VII
List of Tables	X
Acronyms	XI
Organization of chapters	XII

Chapter-1: Introduction

1.1 General	1
1.2 Types of Uranium deposits	1
1.3 Objective of the present study	2
1.4 Research Problem and Methodology	3
1.5 Geophysical methods in Uranium exploration	4
1.5.1 Application of IP/Resistivity in uranium exploration	4
1.5.2 Application of Magnetic method in uranium exploration	5

Chapter-2: Geology of the study area

2.1 Regional geology	8
2.1.1 Alwar Sub Basin	9
2.1.2 Khetri Sub-basin	11

Chapter-3: Methodology

3.1 Geophysical methods	16
3.1.1 Magnetic Method	16
3.1.1a Theory of magnetic method	17

3.1.1b Magnetic properties of rocks	18
3.1.1c Physical property measurement	20
3.1.1d Total field anomaly	23
3.1.1e Noise sources in magnetic survey	23
3.2 IP/Resistivity method	
3.2.1 Induced polarization mechanism	24
3.2.2 Measurements in IP	25
3.2.3 Noise sources in IP	27
Chapter-4: Magnetic Survey	
4.1 Data Acquisition	28
4.2 Principle of Proton Precession Magnetometer	29
4.3 Magnetic Data reduction	
4.3.1 Diurnal correction	30
4.3.2 Magnetic data presentation	31
4.4 Magnetic data processing	
4.4.1 Reduced to pole (RTP) filter	32
4.4.2 Upward continuation filter	33
4.4.3 First vertical derivative filter	33
4.5 Interpretation of magnetic data	
4.5.1 Qualitative interpretation	34
4.5.1a Total magnetic intensity anomaly (TMI) map	34
4.5.1b Reduced to pole (RTP) anomaly map	35
4.5.1c First vertical derivative map	37

4.5.2 Quantitative interpretation	38
4.5.2a Euler Deconvolution	39
4.5.2b Forward modeling of magnetic data	40
4.5.2c Inversion of magnetic data	42
Chapter-5: IP/Resistivity survey	
5.1 IP/Resistivity data acquisition	45
5.2 Principle of IP/Resistivity measurement	46
5.2.1 Time-domain measurements	47
5.3 IP/Resistivity data presentation	48
5.4 Processing of IP/Resistivity data	49
5.5 Interpretation of IP/Resistivity data	50
5.5.1 Quantitative Interpretation	50
5.5.1a Apparent resistivity map	50
5.5.1b Apparent chargeability map	51
5.5.2 Quantitative Interpretation	52
5.5.2a Inversion of Pseudo-depth section data	52
5.5.2b IP decay curve analysis	54
Chapter-6: Global Optimisation: The Particle Swarm Optimisation	
6.1 Global Optimisation approach	57
6.1.1 Particle Swarm Optimisation	59
Chapter-7: Modeling and Inversion	
7.1 2D Forward modeling of Magnetic data	66

7.2 Particle Swarm Optimisation of magnetic data	69
7.2.1 Inference about Particle Swarm optimisation algorithm	73
7.3 Integrated interpretation	73
Chapter-8: Results and Conclusions	75
Future scope of work	77
References	78

SYNOPSIS

This thesis for M. Tech project through HBNI deals with methodological approach in Uranium exploration utilizing geophysical techniques in parts of North Delhi Fold Belt (NDFB), Rajasthan. The study area, Rajpura, is about 11 km WNW of Rohil Uranium deposit, Sikar District, Rajasthan. Detailed geophysical surveys comprising of Magnetic and Induced Polarisation/Resistivity were adopted to address the problem of locating subsurface geologic structures and chargeability zones which are possible locales for U-mineralisation. The magnetic and IP/resistivity data have been acquired over an area of 10.0 and 5.0 sq. km respectively. Data processing was carried out by applying suitable signal enhancement techniques and interpretation of the same was done qualitatively as well as quantitatively.

The qualitative interpretation of magnetic data shows a folded structure trending in NE-SW direction. Based on the trends of the contours and their offsets, faults are marked. Further, qualitative and quantitative interpretation using several advanced tool techniques facilitated in mapping/deciphering sub-surface disposition of the geological domains and structures. From the magnetic data along with the geological inputs from the available outcrop in the area two litho-units are attributed to the magnetic data, i.e. magnetite bearing quartzite and quartz-biotite schist (QBS). The outcrop in the area revealed indications of brittle (fractured/faults) and ductile deformation (shearing). Particle swarm optimisation inversion algorithm was independently written in Python programming language and inversion of the magnetic data was carried out. The PSO algorithm is chosen as it is a derivative free technique and is less sensitive to the nature of the objective function compared to other conventional approaches and heuristic methods (Lee and Park, 2006). It is less dependent of a set of initial points compared to other evolutionary methods, implying that the convergence is robust (Lee and Park, 2006). From the inversion of

magnetic data, it is found that the depth to the top of geological bodies varies from 120 to 200 m and are dipping south easterly with a dip amount ranging from 65° to 75° . Interpretation of IP/Resistivity data shows prominent NE-SW trending high chargeability zones low resistivity zone over a strike length of 2.5 km with a width ranging 300 m to the west of Fathepura. High chargeability of the order 15-30 mV/V over a background value of 8 mV/V is noticed within the low resistivity (100 -200 Ohm-m) zone. The high chargeability values are attributed to the presence of disseminated sulphides in fractured Quartz-Biotite-Schist (QBS) and in sheared contact between QBS and magnetite bearing quartzites. Integrated interpretation of magnetic and IP/Resistivity data successfully delineated high chargeability, low to moderate resistivity and moderate to high magnetic anomaly zone (magnetite bearing quartzite) and are inferred to be potential targets for sub-surface uranium mineralisation in the area, moderate to high magnetic zone with low to moderate resistivity are inferred to be sheared contact between the magnetite bearing quartzite and QBS, correlating with high chargeability suggests the presence of disseminated sulphides which provide a reducing environment for Uranium precipitation.

LIST OF FIGURES

Figure No.	Description	Page No.
2.1	Regional geological map of North Delhi Fold Belt.	09
2.2	Detailed geological map of the study area.	15
3.1	Histogram showing mean values and ranges in susceptibility of common rock types.	20
3.2(a)	Photographs of available outcrops in the area, of Folded Quartzite.	22
3.2(b)	Photograph of available outcrops in the area, of Folded Quartzite, contact of mica schist and quartzite.	22
4.1	Magnetic survey station locations in Rajpura area, NE of Prithivipura, Sikar district, Rajasthan.	29
4.2	Diurnal variation as on 03.01.2020	31
4.3	Total intensity magnetic map of Rajpura area, NE of Prithivipura, Sikar district, Rajasthan.	35
4.4	Reduced to pole (RTP) map of Rajpura area, NE of Prithivipura, Sikar district, Rajasthan.	37
4.5	First vertical derivative (30 m Upward continued) map of Rajpura area, NE of Prithivipura, Sikar district, Rajasthan.	38
4.6	Euler depth solutions of magnetic data from Rajpura area, NE of Prithivipura, Sikar district, Rajasthan.	40
4.7	Predicted anomaly of a thin sheet like structure. Anomaly computed using MAGFORWARD program in PYTHON 3.6.	41
4.8	Flow structure of forward modeling.	42
4.9	Flow structure of inverse modeling/inversion.	43

5.1	IP/ Resistivity survey station locations in Rajpura area, NE of Prithivipura, Sikar district, Rajasthan.	46
5.2	Transmitted and received waveforms in time domain IP survey.	47
5.3	Decay curve response of Induced polarization data.	49
5.4	Apparent resistivity map of the study area.	51
5.5	Apparent chargeability map of Rajpura area, Sikar district, Rajasthan overlain with high chargeability zones.	52
5.6	Inverted depth sections of IP/Resistivity data.	53
5.7	Decaying double exponential fit to observed IP field data.	55
5.8	Decay curve analysis of line AB from chargeability map of Rajpura area, NE of Prithivipura, Sikar district, Rajasthan.	56
6.1	Local and global minimum of a function.	58
6.2	Forward modeling and PSO inversion of a thin sheet like geologic body. (Noise free)	63
6.3	Forward modeling and PSO inversion of a thin sheet like geologic body. (with 5% gaussian noise)	64
6.4	Forward modeling and PSO inversion of multibody anomaly.	65
7.1	2D forward model of magnetic data along profile AB from Rajpura area, NE of Prithivipura, Sikar district, Rajasthan.	67
7.2	2D forward model of magnetic data along profile PQ	68
7.3	2D PSO inversion of magnetic data along profile AA' from Rajpura area, NE of Prithivipura, Sikar district, Rajasthan.	69
7.4	2D PSO inversion of magnetic data along profile BB' from Rajpura area, NE of Prithivipura, Sikar district, Rajasthan.	70

7.5	2D PSO inversion of magnetic data along profile CC' from Rajpura area, NE of Prithivipura, Sikar district, Rajasthan.	70
7.6	PSO inversion of magnetic data across profile AB.	72
7.7	High chargeability contours superimposed over the reduced to pole (RTP) magnetic map.	74

LIST OF TABLES

Table No.	Description	Page No.
2.1	Stratigraphic sequence of the Khetri Copper Belt.	12
2.2	Stratigraphic sequence of the Delhi Super Group of north-eastern Rajasthan.	14
6.1	Observed and computed model parameters using PSO algorithm corresponding to Figure 6.2.	63
6.2	Observed and computed model parameters using PSO algorithm corresponding to Figure 6.3.	64
7.1	Estimated parameters of the fold limb across profile PQ.	68
7.2	Used ranges for the inputs for PSO inversion of profiles AA', BB', CC'.	71
7.3	Swarm parameters used in inversion of magnetic data.	72
7.4	Inversion results and comparison with the GMSYS modeling.	73

Acronyms

AMD: Atomic Minerals Directorate for Research and Exploration

BARC: Bhaba Atomic Research Center

NDFB: North Delhi Fold Belt

QBS: Quartz biotite schist

EGP: Exploration Geophysics

IAEA: International Atomic Energy Agency

IP: Induced Polarization

E-W: East-West

N-S: North-South

NW-SE: North West-South East

2D: Two Dimensional

3D: Three Dimensional

Organization of Chapters

IP/Resistivity and magnetic surveys have been carried out in Prithivipura area, Sikar district, Rajasthan covering an area extent of approximately 5 and 10 sq. km respectively. The results obtained from the interpretation of magnetic and IP/RES data has revealed the structural features which may prove favourable zones for uranium mineralization. The entire work has been organized in 8 chapters.

Chapter: **1** Introduction: Need of uranium exploration, objective of present study and related aspects.

Chapter: **2** Geology of the study area: Regional geology and detailed geology of the study area.

Chapter: **3** Magnetic Survey: Magnetic survey, processing and interpretation.

Chapter: **4** IP/Resistivity Survey: IP/Resistivity survey, processing and interpretation.

Chapter: **5** Global optimisations: Discussion about PSO algorithm and outputs of PSO2D program.

Chapter: **6** Modeling and Inversion: Models from magnetic and IP/Resistivity data done in different software, comparison of results with results of PSO2D and interpretation.

Chapter: **7** Results and discussions: Results of the work and discussion on attributes related in finding plausible locales for U-mineralisation.

CHAPTER – 1

INTRODUCTION

1.1 General

Today, worldwide, 68% of the energy comes from fossil fuels (41 % coal, 21 % gas, 5.5 % oil), 19 % from hydro and only 13.4% from nuclear and other renewable sources. The average electricity consumption in India is about 1100 kWh per person/or household in a year which is far less than the global average (~2500 kWh). (<https://www.world-nuclear.org>). The day to day dependency on electricity is rising which leads to increasing demand of energy/electricity. To achieve this sustainable goal of energy, nuclear electricity is one of the clean options. For nuclear energy, the fuel; uranium is the primary material.

1.2 Types of Uranium deposits

There are 15 types of uranium resources classified on the basis of deposit type by ‘International Atomic Energy Agency’ (IAEA, 2015). These are arranged according to their approximate economic significance-

1. Intrusive deposits
2. Granite-related
3. Polymetallic iron oxide breccia complex
4. Volcanic-related
5. Metasomatite
6. Metamorphite

7. Proterozoic unconformity
8. Collapse breccia pipe
9. Sandstone
10. Paleo quartz-pebble conglomerate
11. Surficial
12. Lignite-coal
13. Carbonate
14. Phosphate
15. Black shale

1.3 Objective of the present study

The objective of the present study is to delineate subsurface geological structures magnetic data and disseminated sulphide rich zones IP/Resistivity data. In NDFB, uranium mineralization is found in fractures within the quartz biotite schist and fractured quartzite associated with sulphides. Magnetic and IP/Resistivity methods are most successful methods in mapping these features. Delineation of geological structures is not only a pre-requisite but also of paramount importance for uranium exploration in areas under soil cover.

In the present study, geophysical investigations were carried out by employing magnetic and IP / electrical resistivity with the objective of delineating structural features/conduits such as faults/fractures or weak zones along with sulphide dissemination respectively. Since sulphides provide a reducing environment for the precipitation of uranium these structural conduits /weak zones with disseminated sulphides are favourable locales for uranium mineralisation.

1.4 Research Problem and Methodology

Previous workers have reported fracture-controlled occurrences of uraniferous metasomatites/albitites near Rohil village in Rajasthan in North Delhi Fold Belt (NDFB) (Yadav et al., 2002). Uranium mineralisation is associated with albitized and pyroxenised metasediments, especially quartz-biotite-schist, carbon phyllite/graphitic schist and metallic sulfides. Uranium mineralisation occurs along steeply dipping contacts/faulted contacts between quartz-biotite-schist and massive quartzite. Characteristic signatures i.e., low magnetic and high chargeability has been provided by ground magnetic and Induced Polarization method (IP) owing to uranium mineralization in the shear zones and delineated strike extension of mineralization (Srinivasa Rao et. al., 2016). The study area, 10 sq. km, around the villages Prithvipura-Gudhakhud is a part of the Khetri sub-basin is around 11 km to the south-west of well-known Rohil uranium deposit. Since the study area lies in a similar geological domain with distinct features, hence warrants magnetic, induced polarisation and resistivity surveys for detailed modeling and interpretation for subsurface uranium exploration. Mapping of subsurface geological structures such as fractures, faults, litho-contacts and shear zones are most important in any mineral exploration. Uranium needs a reducing environment for precipitation and sulphide rich zones are good indicators of reducing environment. IP & resistivity survey facilitates in delineation of these sulphide rich zones. Therefore, Global optimisation approach for magnetic and IP/resistivity data to decipher subsurface structures and conductive zones justify the present study and are planned.

1.5 Geophysical methods in Uranium exploration

1.5.1 Application of Magnetic method in Uranium exploration

The magnetic method is a geophysical method that detects the magnetic intensity at a point on the surface of earth owing the distribution of magnetic minerals in the rock underneath. It is the primary exploration tool in the search for minerals. In other arenas, the magnetic method has evolved from its sole use for mapping basement structure to a wide range of new applications, such as locating intra-sedimentary faults, defining subtle lithologic contacts, mapping salt domes in weakly magnetic sediments, and better defining targets through 3D inversion. These new applications have increased the method's utility in all realms of exploration-in the search for minerals, oil and gas, geothermal resources, and groundwater, and for a variety of other purposes such as natural hazards assessment, mapping impact structures, and engineering and environmental studies (Nabighian et al., 2005).

Ground and airborne magnetic surveys are used at just about every conceivable scale and for a wide range of purposes. In exploration, magnetic surveys historically have been employed chiefly in the search for minerals. Regional and detailed magnetic surveys continue to be a primary mineral exploration tool in the search for diverse commodities, such as iron, base and precious metals, diamonds, molybdenum, and titanium. Historically, ground surveys and today primarily airborne surveys are used for the direct detection of mineralization such as iron oxide–copper–gold (FeO-Cu-Au) deposits, skarns, massive sulphides, and heavy mineral sands; for locating favourable host rocks or environments such as carbonatites, kimberlites, porphyritic intrusions, faulting, and hydrothermal alteration; and for general geologic mapping of prospective areas. Aeromagnetic surveys coupled with geologic insights were the primary tools in discovering the Far West Rand Goldfields gold system, one of the most productive systems in

history (Roux, 1970). Kimberlites (the host rock for diamonds) are explored successfully using high-resolution aeromagnetic surveys (positive or negative anomalies, depending on magnetization contrasts) (Macnae, 1979; Keating, 1995; Power et al., 2004). Another economically important use of the magnetic method is the mapping of buried igneous bodies. These generally have higher susceptibilities than the rocks that they intrude, so it is often easy to map them in plan view. Commonly, the approximate 3D geometry of the body can also be determined. Because igneous bodies are frequently associated with mineralization, a magnetic interpretation can be the first step in finding areas favourable for the existence of a mineral deposit. For regional exploration, magnetic measurements are important for understanding the tectonic setting. For example, continental terrane boundaries are commonly recognized by the contrast in magnetic fabric across the line of contact (Ross et al., 1994; examples in Finn, 2002). Such regional interpretations require continent-scale magnetic databases (Nabighian et al., 2005).

1.5.2 Application of IP/Resistivity method to uranium exploration

Uranium minerals as such do not occur in most of the cases in sufficient quantity or have distinct physical property contrast over the surrounding rocks to provide detectable geophysical anomaly. Direct detection of radioactivity has been the main application in uranium exploration using instruments sensitive to mainly gamma radiation. Gamma radiation emitted by its daughter products can be completely masked by even less than a meter of soil cover. Shallow depth capabilities (a few tens of centimetres) of radioactive prospecting methods are constrained to seek uranium deposits occurring at greater depths. Uranium mineralization does not differ in resistivity from the host environment, and the spatial extent of an ore body is often small, hence the direct detection of uranium by measuring resistivity or conductivity is not feasible. However,

it is possible, to utilize electrical and IP methods to detect subsurface geological targets often associated with uranium mineralization. Frequent association of Uranium mineralization with conducting and magnetic minerals or its presence along fault planes, shear zones, geological contacts and other alteration zones provide opportunities to locate those using geophysical methods (Sundararajan et. al., 2017). Such geological targets include graphitic conductors or other similar stratigraphic units with strong carbonaceous affinities. The contrast in conductivity of the conducting minerals and also structures with the host rocks reflect as anomalies in resistivity and IP parameters. IP methods has successfully delineated vein structures of metal sulphides embedded in Palaeozoic materials underlying a sedimentary cover (Martinez et. al., 2019). Gradient profiling followed by geoelectrical sounding has been found successful to delineate fractures saturated with water in hard rock areas (Yadav and Singh, 2007).

Most of the world uranium deposits are in fact someway or other related to major structural features such as faults, shears and mylonite in the basement rocks. Even a small amount of graphitic material in shear/fracture zones can significantly increase its conductivity.

Fault/fractures within the basement acts as conduits for passage of the hydrothermal solutions and Uranium gets precipitated at the unconformity on encountering any reducing agents such as sulphides, carbon, iron oxides, graphite. Such deposits can be effectively delineated by IP or EM surveys. IP/resistivity surveys have shown potential for detecting sulphides associated with the uranium minerals, for example at the Armchair and Streitberg Ridge prospects in the Mount Painter Inlier (Dentith, 2003). IP surveys are very helpful in delineating uranium mineralized zones indirectly when it associated with even highly disseminated sulphide minerals. The IP method eliminates non-metallic conductivity anomalies and does not respond to resistivity inhomogeneities. Mineral discrimination is possible from the IP data using relaxation time

distribution analysis (RTD). This approach has been applied in Jahaz, Hirapur and Sankadih, India (Kumar et. al., 2019) and has been found to discriminate between sulphides, magnetite and host rock (schist).

Evidently, resistivity/IP methods have become indispensable tools in uranium exploration programs. Design of the survey methodology depends on the type of mineralisation occurrence, associated minerals and geometry of the structural features. Methodology is designed based on the geological problem and the expected anomalous signatures. Vertical to sub-vertical conductors can be best delineated by using dipole-dipole or pole-dipole array whereas Wenner-Schlumberger array is best suited for imaging horizontal to sub-horizontal conductive bodies (Mishra and Shalivahan, 2015).

Study and analysis of multiple physical properties of different rock types in the area along with geophysical responses can resolve the ambiguities in interpretation (Pears and Chalke, 2016). A judicious combination of geophysical methods with proper understanding of the control of uranium mineralization has the capability of maximizing the ratio of mineralized to non-mineralized boreholes in a geologic terrain (Rajaraman et. al., 2011).

CHAPTER – 2

GEOLOGY OF THE STUDY AREA

2.1 Regional geology

Mesoproterozoic Delhi Supergroup forming the major part of Delhi Fold Belt is subdivided into two parts, an older segment to the north of Ajmer, the North Delhi Fold Belt (NDFB) and the relatively younger terrain to the south of Ajmer, the South Delhi Fold Belt (SDFB). These two terrains display distinct characteristics in terms of sedimentary facies, degree of metamorphism and the structural evolution pattern formed during different tectonic events and associated mineralization (Sinha-Roy, 1998).

Delhi Fold Belt is a narrow linear fold belt extending in parts of Rajasthan and Haryana, and it represents the main orographic axis of the states. This linear folded belt is the consequences of different episodes of orographic movements and complex deformations of the rock sequences present in nearly isolated and independent fault bound basins formed during Middle to Upper Proterozoic periods. (Sinha-Roy et. al.,1998). North Delhi Fold Belt is further sub-divided into three sub-basins i.e. Bayana-Lalsot, Alwar and Khetri sub-basins. These are deposited in three grabens separated by horsts from east to west (Singh, 1988). Figure-2.1 shows the regional geological map of North Delhi Fold Belt. All the sub-basins are characterized by the rocks distributed over two major stratigraphic units such as the older arenaceous sediments of Alwar Group grading into the younger argillaceous sediments of the Ajabgarh Group. The stratigraphic sequence of the Delhi Super Group of the north-eastern Rajasthan has been shown in Table-2.2.

The study area falls in Khetri sub-basin, which is the main copper belt, comprising of Paleo to Mesoproterozoic rocks.

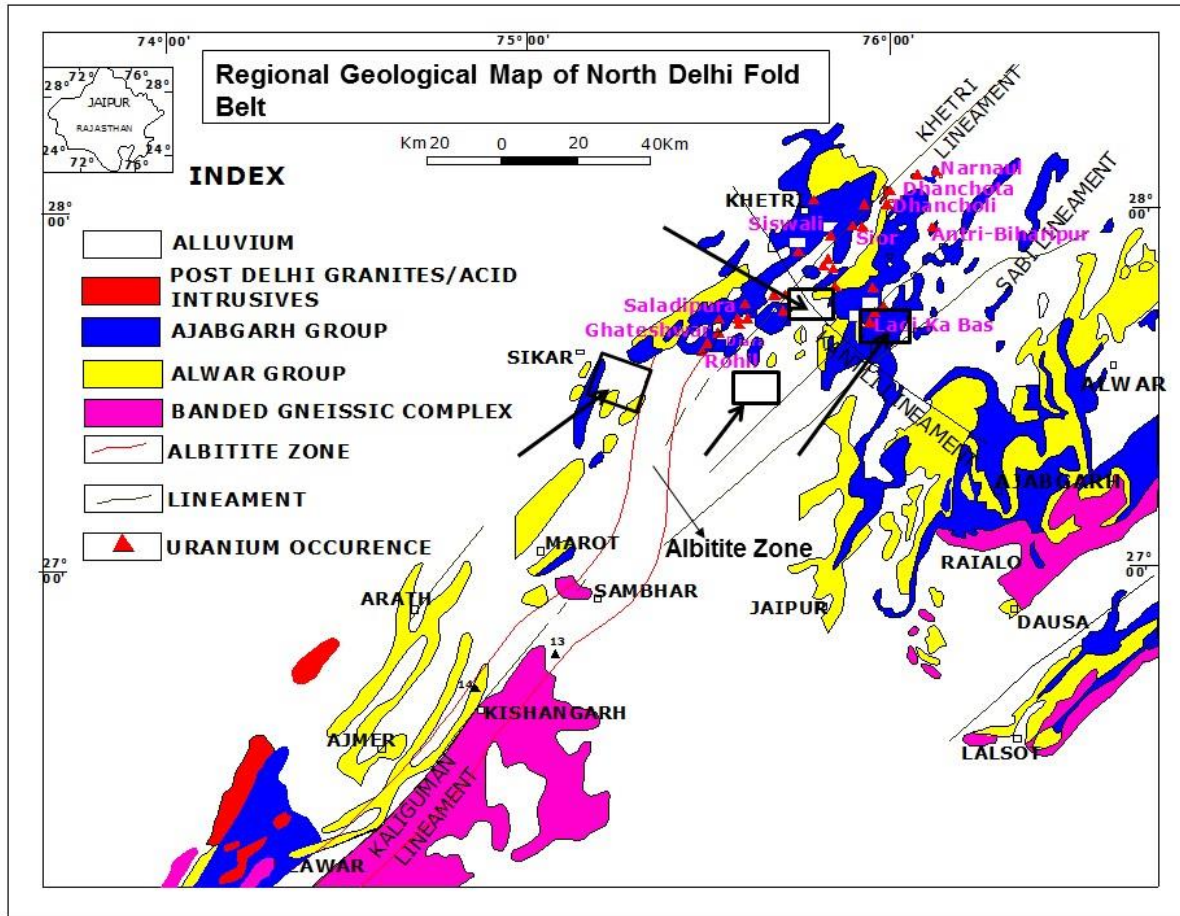


Figure 2.1. Regional geological map of North Delhi Fold Belt. (Modified after GSI, 1995)

Delhi Supergroup of rocks along with the late/post orogenic bodies of granitoids, diorite-tonalite, serpentinite and gabbro-norite-charnockite of diverse ages and basement Pre-Delhi rocks. Delhi Group of rocks unconformably overlie Pre-plains (Heron, 1953). The NDFB is characterized by several fossil grabens and horsts, distributed broadly in three main sedimentary sub-basins.

2.1.1 Alwar Sub-basin

From Jaipur in the south, the Alwar sub-basin extend beyond Rajasthan-Haryana border in the north and is located between the Lalsot-Bayan sub-basin in the east and the Khetri sub-basin

in the west. The Alwar sub-basin tapers southward near Lalgah. This basin is separated from both Khetri and Lalsot-Bayana sub-basins by prominent faults or lineaments. Carbonate sediments of the Dogeta Formation accumulated in shallow basins under stable conditions. Poor clastic content of these sediments suggests that the basin flanks had subdued relief and that there was no major river system to make terrigenous input into the basin.

The Alwar Group sediments were deposited in the Alwar sub-basin in the newly formed basin, i.e., Thatra, east of Surer graben, to the west of Dogeta graben. The dominantly clastic sediments divided into Mortalab quartzite, Mohini conglomerate, Kanawar quartzite and Lakhanpur sandstone, these clastic sediments were deposited in these grabens with an unconformity with the underlying Raialo Group sediments as well as with the pre-Delhi rocks. The sedimentary structures preserved in the form of current bedding and ripple marks suggest braided stream and subtidal to lower tidal-flat environment of deposition.

The Ajabgarh sediments overlying the Alwar clastics with a disconformity are subdivided into Kushalgarh, Seriska, Rajgarh, Kanwari, Thangazi, Kharkol and Arauli-Mandhan Formations. The Seriska Formation contains massive white quartzite with intraformational breccia, carbon phyllite and marble. The Rajgarh Formation is clastic rich, having conglomerate and boulder beds at the base. The carbon phyllite, staurolite bearing carbon phyllite with thin quartzite and marble intercalations are included in the Thanagazi Formation.

The rocks of the Alwar and Lalsot-Bayan sub-basins have suffered three main phases of folding. The early isoclinal folds with NNE-SSW axial traces are over printed by folds having large interlimb angle and steep axial planes. The third generation of folds are mainly represented by broad warps and kinks. The map pattern is controlled by the interference of these folds, resulting in 'hook-shaped' to 'dome and basin' structures (Das, 1988).

The pelitic assemblages of the Alwar sub-basin containing staurolite biotite association along with garnet and/or andalusite suggest metamorphic facies similar to that of the Khetri copper belt (Gangopadhyay and Sen, 1972). The development of the sillimanite in the pelite and scapolite and chondrodite in the marble in the vicinity of granite plutons suggests a late thermal effect of the granite bodies. The absence of kyanite in this belt suggests a lower grade of metamorphism than that in the Khetri copper belt (Sharma, 1988).

2.1.2 Khetri Sub-basin

Khetri sub-basin extends from Singhana in the north to Sangrwa in the south over a distance of 80 km, linear outcrops of clastics, psammopelites and pelitic associations are generally included in the Khetri sub-basin. In the eastern part it is occupied by low and isolated mounds composed of Alwar sub-basin rocks in the Shekhawati plains and sand dunes occupy its western part. The Khetri copper belt consists mainly of psammities of the Alwar Group grading into pelites of the younger Ajabgarh Group, each being about 130 m thick. The Alwar Group comprises pelites, quartzite-arkose and amphibole quartzite along with marble in a young in stratigraphic order. The Ajabgarh Group can be subdivided into pelites of various types, marble, calc-gneisses and quartzite. The stratigraphic order is mainly based on primary sedimentary features and other small-scale structural criteria. The stratigraphy of the Khetri sub-basin is shown in Table 2.1.

The rocks of both Alwar and Ajabgarh Groups are disposed in NE-SW trending large longitudinal folds, the older Alwar rocks occurring in the core of the major anticlines lying beneath the Ajabgarh rocks. Large-scale coaxial folding and associated faulting at the crestal

parts of the Babai anticline have resulted in the juxtaposition of the alternating Alwar and Ajabgarh rocks in the eastern part of the belt.

Table 2.1. Stratigraphic sequence of the Khetri Copper Belt (after Dasgupta, 1968)

	Younger amphibolite chert, ankerite and quartz veins Base metal mineralization and Fe-Mg metasomatism Granites Older amphibolite Unit-8 – Phyllite, schist etc. Unit-7 – Quartzite, phyllite etc. Unit-6 – Phyllite, schist Unit-5 – Marble, calc-gneiss Unit-4 – Types of schist and phyllite
-----Gradational Contact-----	
Alwar Group	Unit-3 – Amphibole quartzite, amphibole gneiss, marble Unit-2 – Quartzite, Arkose Unit-1 – Phyllite, schist (Base not exposed)

The strain history of the rocks of the Khetri sub-basin suggests that a sub horizontal NW-SE shear couple acting on the horizontal beds gave rise to the isoclinal, recumbent to gently plunging reclined first generation of folds with initial NE-SW axial trend. This rotational strain was replaced by a pure shear in a horizontal NW-SE direction resulting in coaxial upright second generation of folds. A third generation of structures are developed because of the release strain accumulated by the second deformation related compression. In the last phase of deformation, the compression direction became N-S and horizontal, signifying a longitudinal shortening (Naha et. al., 1988).

The metasediments of the Alwar and Ajabgarh Groups show structures of similar style and orientation. Large asymmetric doubly plunging folds are developed on regional scale with axial culminations and depressions, having NE-SW trending axial traces. Structures of four generations have been recognized in the Khetri sub-basin rocks (Naha et. al., 1988). The first folds are recumbent or gently plunging reclined folds while the second folds are upright. The third set of folds is represented by kinks and conjugate folds with sub-horizontal to gently dipping axial planes. The fourth generation of folds are characterized by upright conjugate folds with axial planes striking NE-SW and NW-SE and upright folds with axial planes striking E-W. In the northern part of the Khetri belt anticlines and synclines having upright to slightly overturned geometry are the major structures passing westward into the overturned Kolihan syncline. The transverse faults, orthogonal to the major fold axes, are formed during extension and shortening parallel to the fold axes. Large scale transverse faults are developed 5 km NE of Babai and at Chapoli. Shear deformation is the major mechanism for the formation of the majority of the faults in the KCB (Dasgupta, 1968).

Prograde metamorphism in the belt is related to granite intrusion and feldspathisation, and is followed by the retrogression, Fe-Mg-K metasomatism, associated alteration and albitization. Metamorphism prior to basic rock intrusions was of low grade producing only sericite-biotite assemblages. The grade of metamorphism increases towards the eastern part of the KCB where strong deformation is accompanied with granite intrusions. In the southern part of the Khetri Copper Belt widespread occurrence of Albitite have been reported; the albitites have intruded the metasediments of the Delhi Supergroup and Post Delhi (?) (Ray, 1987). Uranium mineralisation (in the form of mineral brannerite) has been reported from the Khandela area (Dar, 1964).

Group	Formation	Lithology
Ajabgarh	Acid intrusive Basic intrusive Arauli-Mandhan Formation Bharkol Formation Thana-Ghazi Formation Seriska/Weir Formation Kushalgarh Formation	Granite, Pegmatite and Quatrz veins Amphibolite and metadolerite Quartzite, stauralite-garnet schist, carbon phyllite, slate Quartzite with interbedded phyllite and carbon phyllite Carbon phyllite, tuffaceous phyllite, sericite, schist, quartzite and marble Brecciated and ferruginous quartzite, chert, breccia, carbon phyllite and marble Impure marble with lenses of phosphorite, basic flows, agglomerate tuff
~~~~~Unconformity~~~~~		
Alwar	Pratapgarh Formation (=Bayana and Damdama formations)  Kankwarhi Formation (= Badalgarh Formation)  Rajgarh Formation (=Jogipura Formation)	Quartzite and quartz-sericite (Conglomerate)  Quartz-sericite schist, quartzite schist, quartzite with thin lenses of marble and conglomerate  Quartzite, marble, gritty quartzite, conglomerate
~~~~~Unconformity~~~~~		
Railo	Thela Formation (= Bayana and Damdama Formations) Serrate Quartzite (= Nithar Formation) DogetaFormation	Lava flow, pillow lava, agglomerate, spatter, pyroclastic breccia, tuff, epiclastic breccia and associated conglomerate, quartzite, schist, phyllite, marble. Quartzite with wedge and lenses of oligomictic conglomerate. Banded siliceous marble, quartzite phyllite, dolomitic marble with bands of conglomerate, quartzite phyllite and schist.
~~~~~Unconformity~~~~~		
Pre-Delhi		Granite and gneisses, amphibolite, quartzite, phyllite, schist, marble, banded magnetite-hematite-jasper, tuff. Granitized meta-sediments

Table 2.2. Stratigraphic sequence of the Delhi Super Group of north-eastern Rajasthan (after Banerjee, 1980; Singh, 1988).

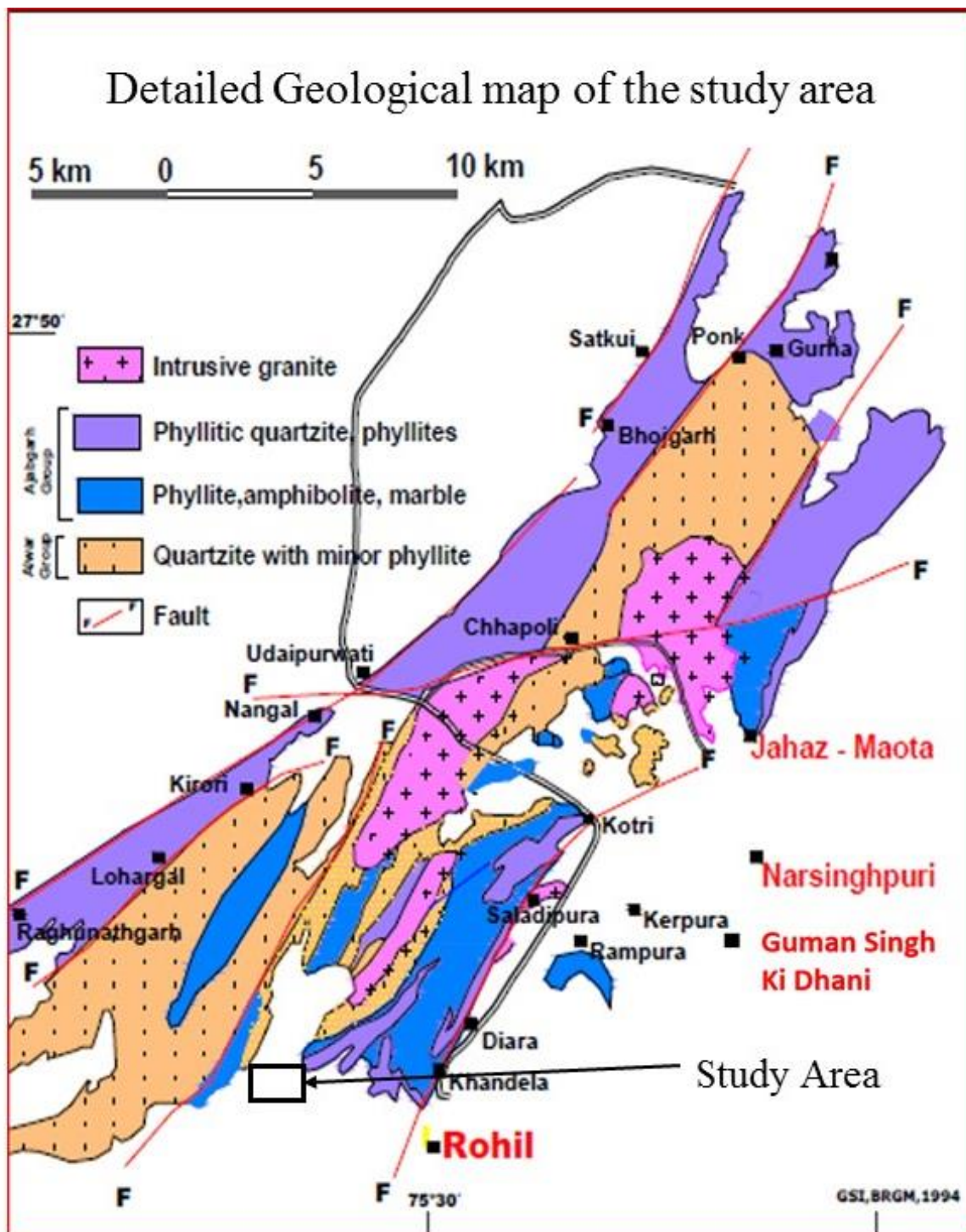


Figure 2.2. Detailed geological map of the study area.

## **CHAPTER-3**

### **METHODOLOGY**

#### **3.1 Geophysical methods**

The geophysical methods are employed to get the earth response in terms of various physical parameters owing to the physical property contrast within the earth, such as density, magnetic susceptibility, electrical resistivity, conductivity and chargeability. Geophysical methods act as an indirect tool for the delineation of possible subsurface locales for uranium mineralization. Interpretation of geophysical data helps in deciphering faults, fractures, alteration zones, mineralised zones and any geologic structures. Often uranium mineralization is found to be associated with sulfides since sulfides provide a reducing environment for uranium to precipitate. Geophysical methods involving magnetic and IP/resistivity are used to indirectly decipher for such locales in the subsurface.

##### **3.1.1 Magnetic Method**

The aim of the magnetic survey is to investigate subsurface geology on the basis of anomalies in the Earth's magnetic field resulting from the magnetic properties of the underlying rocks. Magnetic surveying thus has a broad range of applications, from small scale engineering or archaeological surveys to detect buried metallic objects, to large-scale surveys carried out to investigate regional geological structure. Magnetic surveys can be performed on land, at sea and in the air. Consequently, the technique is widely employed, and the speed of operation of airborne surveys makes the method very attractive in the search for types of ore deposit that contain magnetic minerals (Kearey et al. 2002).

### 3.1.1a. Theory of Magnetic method

A freely suspended bar magnet similarly aligns in the flux of the Earth's magnetic field. The pole of the magnet which tends to point in the direction of the Earth's north pole is called the north-seeking or positive pole, and this is balanced by a south-seeking or negative pole of identical strength at the opposite end of the magnet. The force  $F$  between two magnetic poles of strengths  $m_1$  and  $m_2$  separated by a distance  $r$  is given by-

$$F = \mu_0.m_1.m_2 / 4.\pi. \mu_r. r^2 \quad \text{Eq. (3.1)}$$

where,  $\mu_0$  and  $\mu_r$  are constants corresponding to the magnetic permeability of vacuum and the relative magnetic permeability of the medium separating the poles (see later). The force is attractive if the poles are of different sign and repulsive if they are of like sign. The magnetic field  $B$  due to a pole of strength  $m$  at a distance  $r$  from the pole is defined as the force exerted on a unit positive pole at that point

$$B = \mu_0.m / 4.\pi. \mu_r. r^2 \quad \text{Eq. (3.2)}$$

Magnetic fields can be defined in terms of *magnetic potentials* in a similar manner to gravitational fields. For a single pole of strength  $m$ , the magnetic potential  $U$  at a distance  $r$  from the pole is given by

$$U = \mu_0.m / 4.\pi. \mu_r. r \quad \text{Eq. (3.3)}$$

The magnetic field component in any direction is then given by the partial derivative of the potential in that direction (Kearey et al. 2002).

The terrestrial magnetic field is the summation of several magnetic components, derived from both within and outer side the earth, which vary spatially and temporally over and above the Earth. The main field generated by electromagnetic currents in the outer core of the earth accounts for about 98% or more of the geomagnetic field.

The geomagnetic field can be described in terms of the Declination (D), Inclination (I), and the total field vector (F). The magnetic intensity of the Earth's magnetic field varies with latitude, from a minimum of around 28,000 nT at the magnetic equator to 68,000 nT at the magnetic poles. The magnetic vector can be expressed as Cartesian components parallel to any three orthogonal axes. The geomagnetic elements are taken to be components parallel to the geographic north and east directions and the vertically downward direction. Alternatively, the geomagnetic elements can be expressed in spherical polar coordinates. The magnitude of the magnetic vector is given by the field strength  $F$ ; its direction is specified by two angles. The declination (D) is the angle between the magnetic meridian and the geographic meridian; the inclination (I) is the angle at which the magnetic vector dips below the horizontal.

The magnetic field of the Earth is a vector, that is, it has both magnitude and direction. The magnitude, or intensity  $F$ , of the field is measured in the same units as other B fields, namely in Tesla. However, a Tesla is an extremely strong magnetic field, such as one would observe between the poles of a powerful electromagnet. The Earth's magnetic field is much weaker; its maximum intensity is reached near to the magnetic poles, where it amounts to about  $6 \times 10^{-5}$  T. Modern instruments for measuring magnetic fields (called magnetometers) have a sensitivity of about 0.01 T; this unit is called a nanotesla (nT) and has been adopted in geophysics as the practical unit for expressing the intensity of geomagnetic field intensity.

### **3.1.1b. Magnetic properties of rocks**

Most common rock-forming minerals exhibit a very low magnetic susceptibility and rocks owe their magnetic character to the generally small proportion of magnetic minerals that they contain. There are only two geochemical groups which provide such minerals. The iron–

titanium–oxygen group possesses a solid solution series of magnetic minerals from magnetite ( $\text{Fe}_3\text{O}_4$ ) to ulvöspinel ( $\text{Fe}_2\text{TiO}_4$ ). The other common iron oxide, hematite ( $\text{Fe}_2\text{O}_3$ ), is anti-ferromagnetic and thus does not give rise to magnetic anomalies unless a parasitic anti-ferromagnetism is developed. The iron–sulphur group provides the magnetic mineral pyrrhotite ( $\text{FeS}_{1+x}$ ,  $0 < x < 0.15$ ) whose magnetic susceptibility is dependent upon the actual composition. By far the most common magnetic mineral is magnetite, which has a Curie temperature of  $578^\circ\text{C}$ . Although the size, shape and dispersion of the magnetite grains within a rock affect its magnetic character, it is reasonable to classify the magnetic behaviour of rocks according to their overall magnetite content. A histogram illustrating the susceptibilities of common rock types is presented in Figure 3.1.

Basic igneous rocks are usually highly magnetic due to their relatively high magnetite content. The proportion of magnetite in igneous rocks tends to decrease with increasing acidity so that acid igneous rocks, although variable in their magnetic behaviour, are usually less magnetic than basic rocks. Metamorphic rocks are also variable in their magnetic character. If the partial pressure of oxygen is relatively low, magnetite becomes re-absorbed and the iron and oxygen are incorporated into other mineral phases as the grade of metamorphism increases. Relatively high oxygen partial pressure can, however, result in the formation of magnetite as an accessory mineral in metamorphic reactions (Kearey et al. 2002).

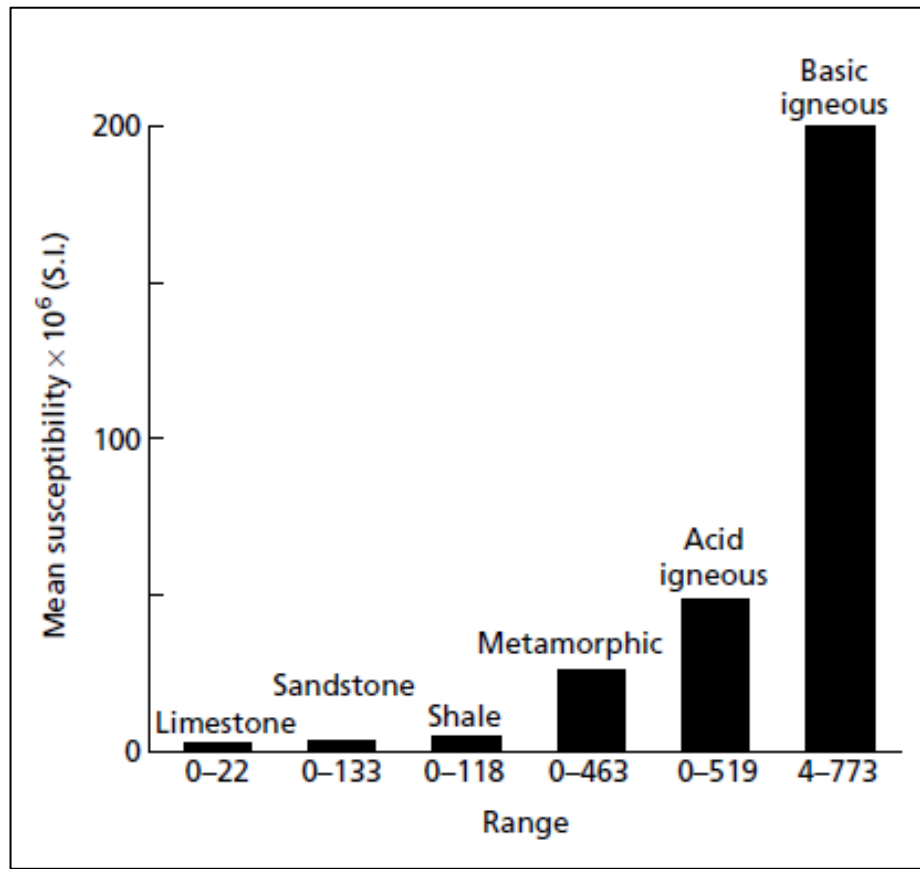


Figure 3.1. Histogram showing mean values and ranges in susceptibility of common rock types. (After Dobrin and Savit, 1988).

### 3.1.1c Physical property measurements

Magnetic method is sensitive to physical property variations i.e., magnetic susceptibilities of minerals in rock formations, so that an appreciation of the factors that affect magnetic susceptibility which will aid in the interpretation of magnetic field data. In this regard magnetic susceptibility measurements are taken over available outcrops in the study area by using KT-10 susceptibility meter (<https://mountsopris.com/kt-10-magnetic-susceptibility-and-conductivity-meters>). Measured magnetic susceptibility of the grab samples are shown in the table. The rock exposures of quartzite, magnetite bearing quartzite and mica schist are observed in the study

area. Some photographs of quartzite and quartzite with mica schist are shown in Figure 3.2(a) and 3.2(b). Few quartz veins have also been observed at places.

Following observations were made from measured values.

- Quartzite shows low order of magnetic susceptibility values while magnetite bearing quartzite gives high magnetic susceptibility values.
- Mica schist records low order of susceptibility values than quartzite.

<b>Sn. No.</b>	<b>Rock type</b>	<b>No of samples (n)</b>	<b>Magnetic susceptibility (K x 10⁻³ SI units)</b>
1.	Quartzite	15	0.05-0.6
2.	Magnetite bearing Quartzite	10	3-35
3.	Mica Schist	10	0.03-0.3

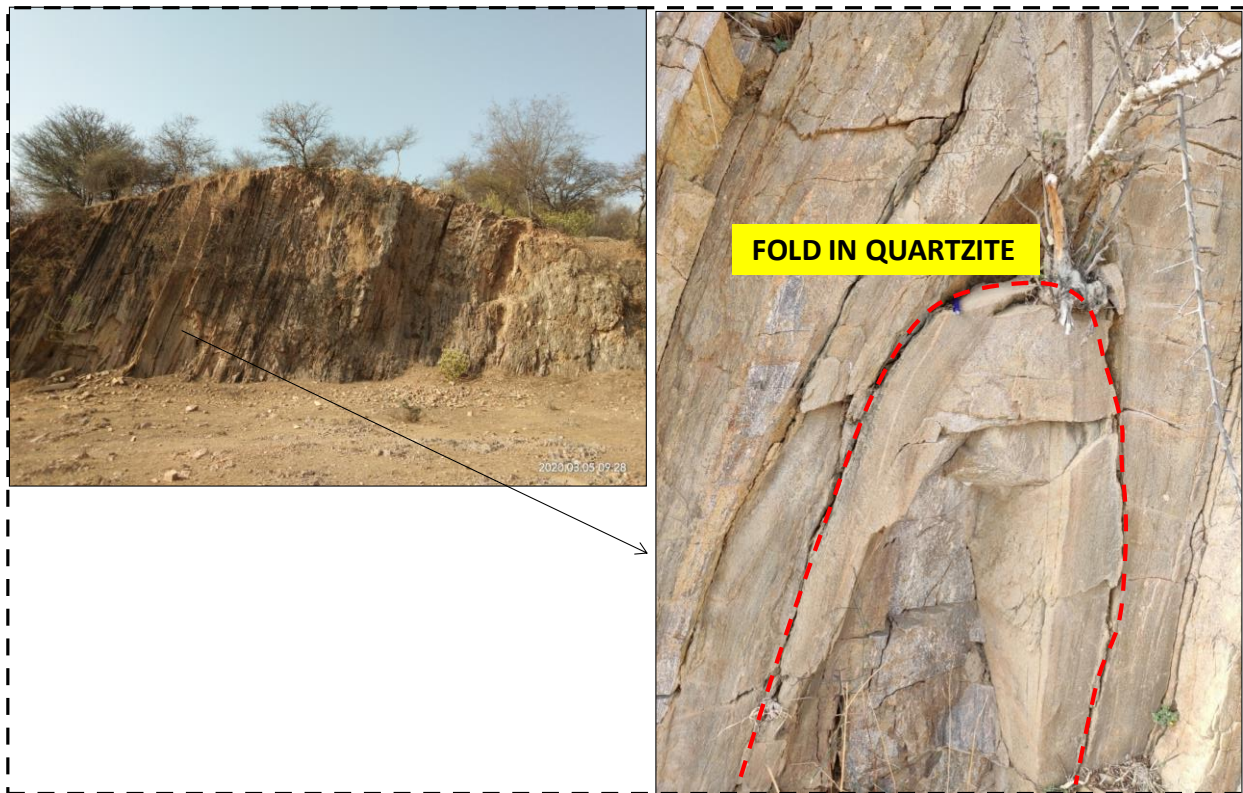


Figure 3.2(a). Photograph of available outcrops in the area, of Folded Quartzite.

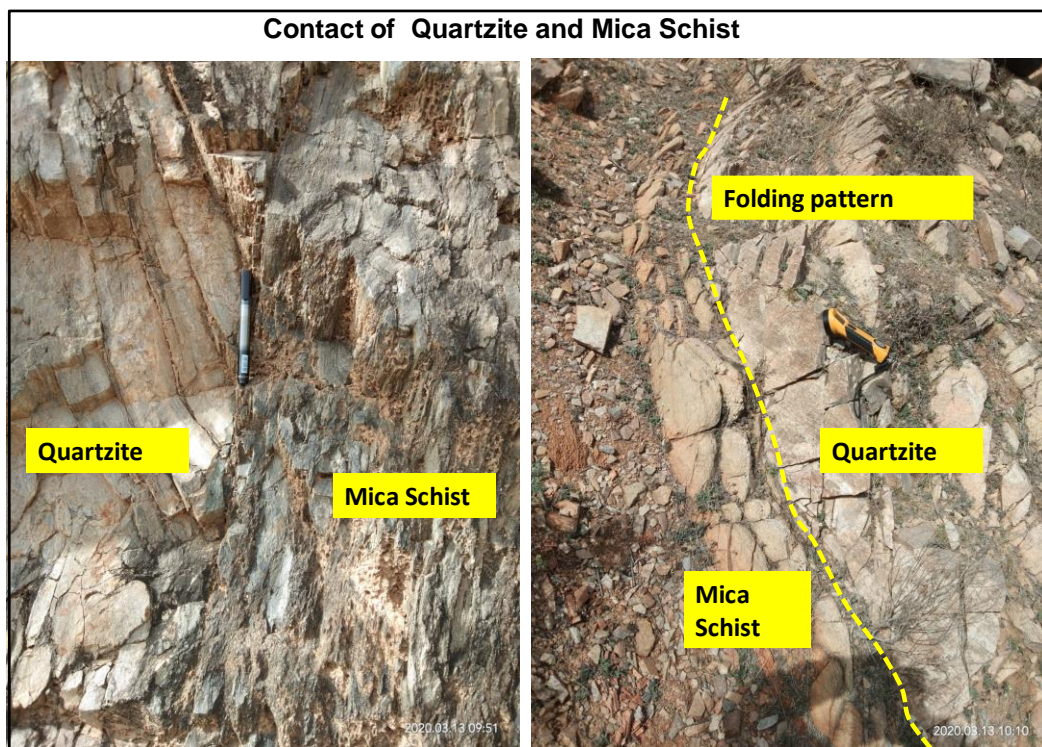


Figure 3.2(b). Photograph of available outcrops in the area, of Folded Quartzite, contact of mica schist and quartzite.

### 3.1.1d. Total field anomaly

Total-field magnetometers measure the magnitude of the total magnetic field without regard to its vector direction. The *total-field anomaly* is calculated from total-field measurements by subtracting the magnitude of a suitable regional field, usually the IGRF model appropriate for the date of the survey. If  $T$  represents the total field at any point, and  $F$  is the regional field at the same point, then the total-field anomaly is given by  $\Delta T = |T| - |F|$ . If the ambient field is much larger than the perturbing field,  $\Delta T$  is approximately equal to one component of the field produced by the anomalous magnetic sources, namely the component in the direction of the regional field.

### 3.1.1.e. Noise Sources in magnetic survey

- Cultural noise: Can be avoided by diverting from the noise source such as high-tension power lines, fences, metallic objects etc.
- Magnetic storms: These are external noise sources that can arise due to the irregular solar activities. These can be removed by employing a base magnetometer and latter applying base correction to the field data.
- Near surface inhomogeneities: These appear as high frequency in the recorded signal. They can be removed by keeping the sensor at a height from the ground or during the processing step by applying a low pass filter.

## 3.2 IP/Resistivity method

### 3.2.1 Induced polarization mechanism

Induced Polarization (IP) is a current-induced electrochemical phenomenon observed as delayed voltage response in earth materials for exploring subsurface mineral deposits. The IP refers to an action of a resistive blocking in earth materials and the process is more pronounced in fluid-filled pores next to metallic minerals (Marshall and Madden, 1959; Sumner, 1976). The IP anomalies are mainly caused by the metallic minerals such as disseminated sulphides and graphite or by the oxides such as magnetite (Telford, 1990). The economic importance in exploration necessitates the discrimination of causative sources from the observed IP response. Laboratory experiments indicate that electrical energy is stored in rocks mainly by electrochemical processes. This is achieved in two ways. The passage of current through a rock as a result of an externally imposed voltage is accomplished mainly by electrolytic flow in the pore fluid. Most of the rock forming minerals have a net negative charge on their outer surfaces in contact with the pore fluid and attract positive ions onto this surface. The concentration of positive ions extends about 100 mm into the pore fluid, and if this distance is of the same order as the diameter of the pore throats, the movement of ions in the fluid resulting from the impressed voltage is inhibited. Negative and positive ions thus build up on either side of the blockage and, on removal of the impressed voltage, return to their original locations over a finite period of time causing a gradually decaying voltage. This effect is known as *membrane polarization* or *electrolytic polarization*. It is most pronounced in the presence of clay minerals where the pores are particularly small. The effect decreases with increasing salinity of the pore fluid. When metallic minerals are present in a rock, an alternative, electronic path is available for current flow. In a rock when metallic mineral grain blocks a pore, when a voltage is applied to

either side of the pore space, positive and negative charges are imposed on opposite sides of the grain. Negative and positive ions then accumulate on either side of the grain which are attempting either to release electrons to the grain or to accept electrons conducted through the grain. Consequently, ions accumulate on either side of the grain and cause a build-up of charge. When the impressed voltage is removed the ions slowly diffuse back to their original locations and cause a transitory decaying voltage.

This effect is known as *electrode polarization* or *overvoltage*. All minerals which are good conductors (e.g. metallic sulphides and oxides, graphite) contribute to this effect. The magnitude of the electrode polarization effect depends upon both the magnitude of the impressed voltage and the mineral concentration. It is most pronounced when the mineral is disseminated throughout the host rock as the surface area available for ionic–electronic interchange is then at a maximum.

### **3.2.2 Measurements in IP**

IP measurements can be acquired using the same four-electrode geometry that is conventionally used for electrical resistivity surveys, although IP surveys typically employ non polarizing electrodes. IP Surveys can be conducted in the time domain as well as in the frequency domain. In the time domain, the current is injected and the decay of the voltage over time is measured. Frequency-domain methods measure the impedance magnitude and phase shift of the voltage relative to an injected alternating current. Spectral induced polarization (SIP) methods measure the polarization relaxation over a range of frequencies (typically over the range of 0.1–1000 Hz) (Hubbard and Linde, 2011). Time-domain IP measurements involve the monitoring of the decaying voltage after the current is switched off. The most commonly

measured parameter is the *chargeability*  $M$ , defined as the area  $A$  beneath the decay curve over a certain time interval  $(t_1-t_2)$  normalized by the steady-state potential difference  $\Delta V_c$ .

$$M = \frac{1}{\Delta V_c} \int_{t_1}^{t_2} v(t) dt$$

Chargeability is measured over a specific time interval shortly after the polarizing current is cut off. The area  $A$  is determined within the measuring apparatus by analogue integration. Different minerals are distinguished by characteristic chargeabilities, for example pyrite has  $M = 13.4$  ms over an interval of 1 s, and magnetite 2.2 ms over the same interval. The current polarity is reversed between successive measurements in order to destroy any remanent polarization and nullify the telluric currents.

Frequency-domain techniques involve the measurement of apparent resistivity at two or more alternate current AC frequencies. IP measurements are usually made at frequencies at 0.1 Hz to below, 10 Hz to remain in the non-inductive regions. Two measurements are commonly made. The *percentage frequency effect* (PFE) is defined as-

$$PPE = 100 \frac{(\rho_{0.1} - \rho_{10})}{\rho_{10}}$$

Where,  $\rho_{dc}$  and  $\rho_{ac}$  are the apparent resistivities measured at 0.1 Hz and 10 Hz respectively.

The *metal factor* (MF) is defined as-

$$MF = 2\pi \times 10^5 \frac{(\rho_{dc} - \rho_{ac})}{\rho_{dc}\rho_{ac}}$$

This factor normalizes the PFE with respect to the lower frequency resistivity and consequently removes, to a certain extent, the variation of the IP effect with the effective resistivity of the host rock.

### 3.2.3 Noise sources in IP

The main noise sources in the Induced polarization survey are discussed as follows:

- The phenomenon of coupling of the transmitter to the receiver through cable-ground or cable-cable capacitance. Capacitive coupling can occur in three ways:
  - i) Capacitive leakage current from the transmitting cable can be picked up by the receiver electrode.
  - ii) Current from the transmitting electrode can capacitively leak into receiving wire.
  - iii) Current can leak directly from wire to wire.

The capacitive coupling is usually small enough to be neglected, unless the insulation of the cables is not proper or the wires lie very close to electrodes other than their own (Bhattacharya and Shalivahan, 2016).

- Electromagnetic coupling between grounded cables gives rise to frequency dependence of resistivity and hence results in spurious anomalies in induced polarization (IP) surveys. It results from the mutual impedance  $Z(\omega) = \frac{V}{I}$  between the current electrodes having  $I$  alternating current through these electrodes, and  $V$  is the electromotive force (emf) between the potential electrodes, both directly and through the ground in their vicinity.

To reduce these effects, current frequency is kept small usually below 10 Hz and current and potential wires are laid far away from each other. Double-dipole and pole-dipole spreads are employed to reduce EM coupling due to long wires.

## **CHAPTER-4**

### **MAGNETIC SURVEY**

#### **4.1 Data Acquisition**

Magnetic data acquisition was carried out in a grid with 100 m line spacing and 25 m station spacing to get maximum geological information (Figure-4.1). Optimum grid size was chosen to avoid spatial aliasing (Boa et. al., 2020) or over sampling. The survey was carried out using Global Positioning System (GPS) based GEM proton precession magnetometers ([www.gemsystem.com](http://www.gemsystem.com)). The GEM magnetometer measures total magnetic field intensity with the sensitivity of 0.1 nT. It has different features like highly effective proton energization. The magnetometer has inbuilt memory which can store as much as data up to 32 Megabytes along with spatial locations using GPS receiver attached to it with a resolution 0.6 m. Diurnal variations of earth's magnetic field were recorded at every 60 second interval using a base station (Location: 27.5168027, 75.3944771) magnetometer. The traverse direction was chosen to be E-W as the general geologic strike of the area is in NNE-SSW. The base station to record the diurnal variations was chosen in a magnetic quiet environment so as not to contribute any spurious value to the calculated anomaly after base correction.

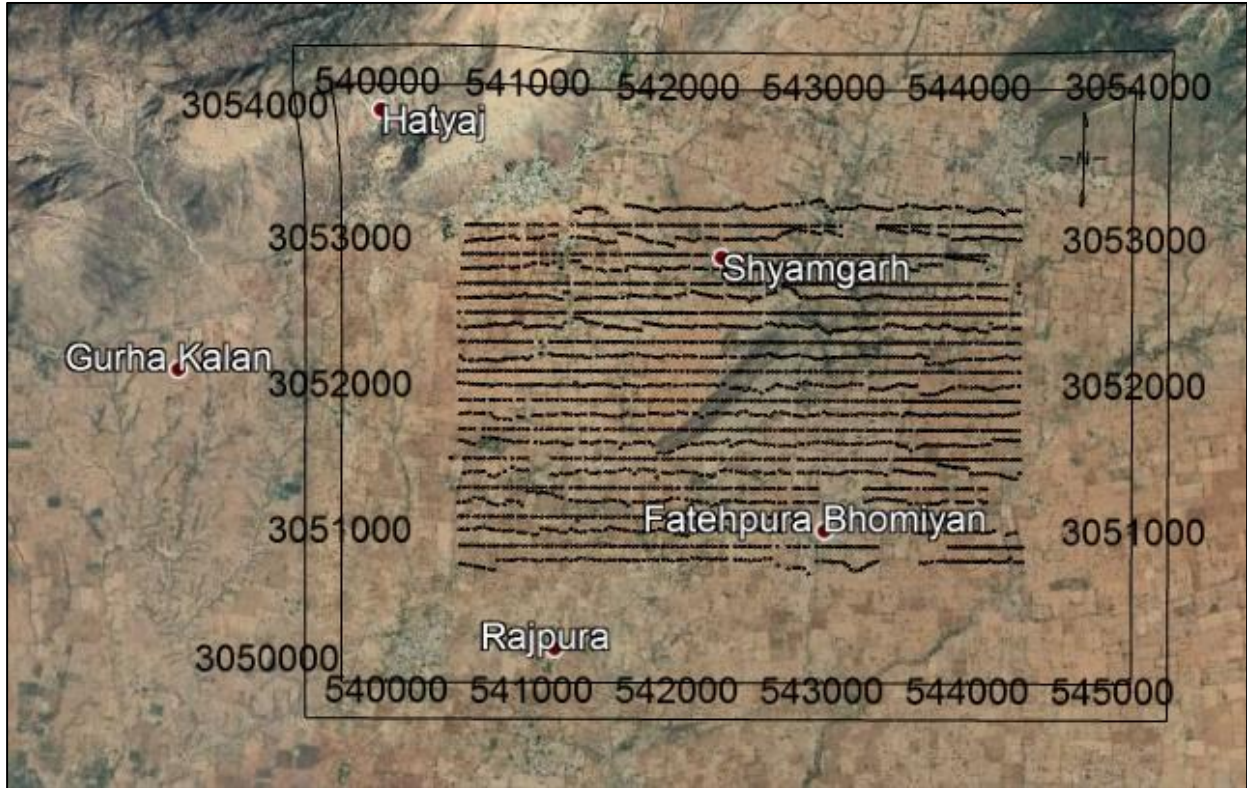


Figure 4.1. Magnetic survey station locations in Rajpura area, NE of Prithivipura, Sikar district, Rajasthan.

## 4.2 Principle of Proton Precession Magnetometer

The proton precession magnetometer has an accuracy of the order 0.1nT to 1nT, it measures the precession frequency, Larmor frequency of the protons in a hydrogen rich fluid that is oriented at a large angle to the geomagnetic field by a strong DC magnetic field originating from a current passing through a wire coil wound around the fluid container, the sensor. When the current through the coil is terminated the relaxation of the applied magnetic field along which the protons of hydrogen align, the protons act as tiny spinning bar magnets precessing around the ambient magnetic field at a frequency dependent on the intensity of the ambient magnetic field related through a constant called, the gyromagnetic ratio of protons. The precessing frequency is given by-

$$f = \frac{\gamma_p B_e}{2\pi}$$

The precessing protons induce a signal within few seconds. The frequency of the induced signal due to the precession of the protons is generally of the order of a few thousand hertz and is measured using a frequency counter. The amplitude of the induced precession is directly dependent on the orientation of the axis of the sensor coil and the direction of the total field. Maximum signal is received when there is a right-angle relationship between the two. No signal is received if the sensor axis and the total field are parallel.

The proton precession magnetometer is subject to erroneous observations caused by power lines, cultural noise, fences etc. interference and large magnetic gradients which produce an incoherent precession signal across the fluid container. Gradients of about 300 nT/m or more, which may occur near highly magnetic natural or man-made materials, will cause the instrument to give spurious readings. Caution has been taken to minimise the noise levels while taking measurements.

### **4.3 Magnetic Data reduction**

The observed data is a culmination of the earth's magnetic field, crustal field, diurnal variation and random noise. The data reduction process is important in the sense so as to minimize the interpretation of artifacts due to random noise. The detailed description of the data reduction is given below.

#### **4.3.1 Diurnal correction**

Diurnal correction is applied to the magnetic data to correct for the temporal variations in the geomagnetic field due to solar activity. Diurnal correction was applied to the acquired data using

the data from the base magnetometer using the GEM link software. The diurnal correction is carried out by comparing the regional magnetic field value of the study area and subtracting those diurnal values synchronized to the field magnetic values using inbuilt GEM link software.

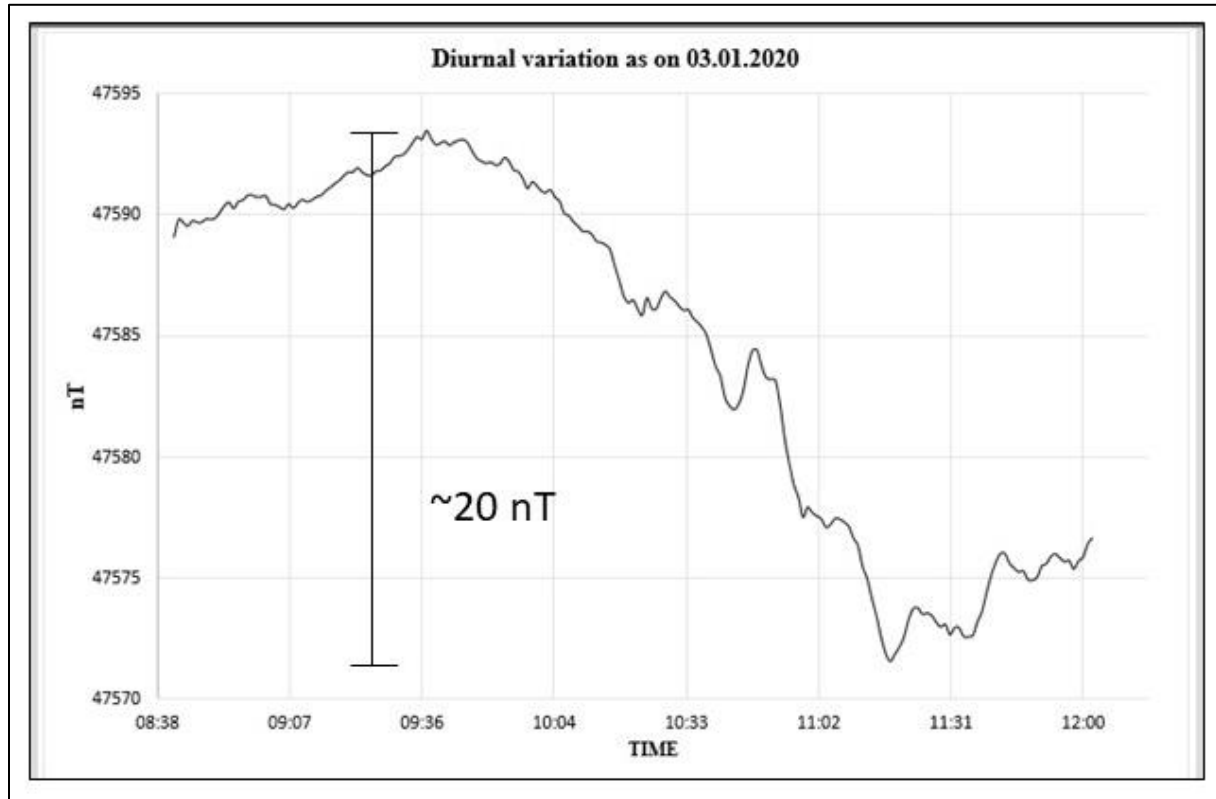


Figure 4.2. Diurnal variation as on 03.01.2020

An average of total magnetic field variation in study area for a particular location in a day is about 15nT. The recorded diurnal variation for a day (03-01-2020) is shown in Figure-4.2.

#### 4.3.2 Magnetic data representation

After preliminary processing, a sequence of steps is required to show the results into an image or profile of the anomalous magnetic field. The first stage of data processing is to remove single-station spikes. For an effective interpretation of magnetic data, several mathematical signal enhancements techniques are used to as per the requirement to get a noise free data. After

all the necessary corrections, the data was processed and presented as 2D images using suitable gridding method and mapping in Oasis Montaj software ([www.geosoft.com](http://www.geosoft.com)) (Figure 4.3 to 4.6). For 2D visualization, the total magnetic field intensity data were gridded using minimum curvature gridding method with a cell size of 25 m. Modelling has been done on observed data by using Model vision software and results are presented in 2-dimensional depth section. Further an inversion algorithm i.e. Particle swarm optimisation algorithm (Kennedy et. al., 1995) was developed in PYTHON environment and modeling was done using the developed computer program both for single source anomaly as well as multi source anomalies. The comparison of the inversion results with the modeling done using commercial software is also carried out.

## **4.4 Magnetic data processing**

### **4.4.1 Reduced to pole (RTP) filter**

If the magnetization and ambient field are not vertical, a symmetrical distribution of magnetization (for example a uniformly magnetized sphere) will produce a skewed rather than a symmetrical magnetic anomaly. This complexity can be removed by applying the reduced to pole (RTP) filter. The effect of RTP filter is to transform a measured total field anomaly into the vertical component of the field caused by the same source distribution magnetized in the vertical direction. The transformed anomaly in the Fourier domain is given by  $F[\Delta T_r] = F[\varphi_r] \cdot F[\Delta T]$ , where  $\Delta T_r$  is the field as measured in the north pole,  $\varphi_r$  contains the phase information of the signal and  $\Delta T$  is the measured field. The application of  $F[\varphi_r]$  is called the ‘reduced to pole’ (Baranov and Naudy, 1964). Reduction to the pole removes one level of complexity from the interpretive process: It shifts anomalies laterally to be located over their respective sources and alters their shape so that symmetrical sources cause symmetrical anomalies.

#### 4.4.2 Upward continuation filter

Upward continuation transforms the potential field measured on one surface to the field that would be measured on another surface farther from all sources. As we shall see, this transformation attenuates anomalies with respect to wavelength, the shorter the wavelength, the greater the attenuation. In this sense, the process of upward continuation degrades the measured data, and we might wonder why such a process would have any application at all. Several useful examples come to mind. It is sometimes necessary to compare or merge aerial surveys measured at disparate altitudes, and upward continuation provides a way to transform individual surveys onto a consistent surface. Second, upward continuation tends to accentuate anomalies caused by deep sources at the expense of anomalies caused by shallow sources. A magnetic survey over young volcanic terrain, for example, may be dominated by short-wavelength anomalies due to near-surface volcanic rocks; upward continuation can be used to attenuate the shallow-source anomalies in order to emphasize deeper, more profound sources, such as underlying plutonic rocks.

If the potential field  $U$  measured on surface  $Z = Z_0$  and has a Fourier transform  $F[U]$ , then in the Fourier domain the upward continuation can be computed using the equation

$$F[U_u] = F[U].e^{-\Delta z.|K|} \quad \text{Eq. (4.1)}$$

The upward continued data obtained from Eq. (4.1) is in Fourier domain and inverse Fourier transform operation reverts back the data to spatial domain (Blakely, 1995).

#### 4.4.3 First vertical derivative filter

First vertical derivative is the vertical gradient of magnetic data. This filter is used to enhance the shallow subsurface features and resolve the closely spaced bodies. This filtering

technique can be applied to both TMI (Total magnetic Intensity) and RTP (Reduced to Pole) data. In the Fourier domain the first vertical derivative is computed using the equation-

$$F \left[ \frac{\partial U}{\partial z} \right] = |K|.F[U] \quad \text{Eq. (4.2)}$$

After computation, an inverse Fourier transform operation would get the data back to spatial domain (Blakely, 1995).

## **4.5 Interpretation of magnetic data**

Data interpretation involves the description of the geophysical anomalies in terms of geological domains. It also involves delineation of anomaly trends, structural features like faults/fractures and depth estimation of causative source bodies. The interpretation of magnetic data is classified in two types- Qualitative interpretation and Quantitative interpretation.

### **4.5.1 Qualitative interpretation**

Qualitative interpretation involves the description of the survey results and to offer explanation to the major and minor anomaly trends and features revealed by a survey in terms of broad geological domains and structures that give rise to the evident anomalies.

#### **4.5.1a. Total magnetic intensity (TMI) anomaly map**

The TMI map was derived from the diurnal corrected magnetic data using the Geosoft, Oasis Montaj software with a grid cell size of 25 m and minimum curvature gridding algorithm (Figure 4.3).

The general trend of the magnetic anomalies in the study area observed in TMI map is in NE-SW direction. Short wavelength high amplitude magnetic anomalies have been identified

towards north of Rajpura and Fathepura. Distinct bi-polar magnetic anomalies trending in ENE-WSW in the north-west corner to NE-SW trend in the central part and around Rajpura and Fathepura are noticed. Amplitudes of the anomaly ranges from -690 to 1040 nT. This linear magnetic trend defines a folded structure of magnetite bearing quartzite in the area with fold axis in NE-SW direction. Discontinuities/breaks in the contours defines the fault/fractures across the limbs of the fold, which is marked in the TMI anomaly map.

The causative source of high magnetic anomalies is attributed to magnetite bearing quartzite. Quartzite ridge which has contact with mica schist has also been observed over high magnetic folded limb.

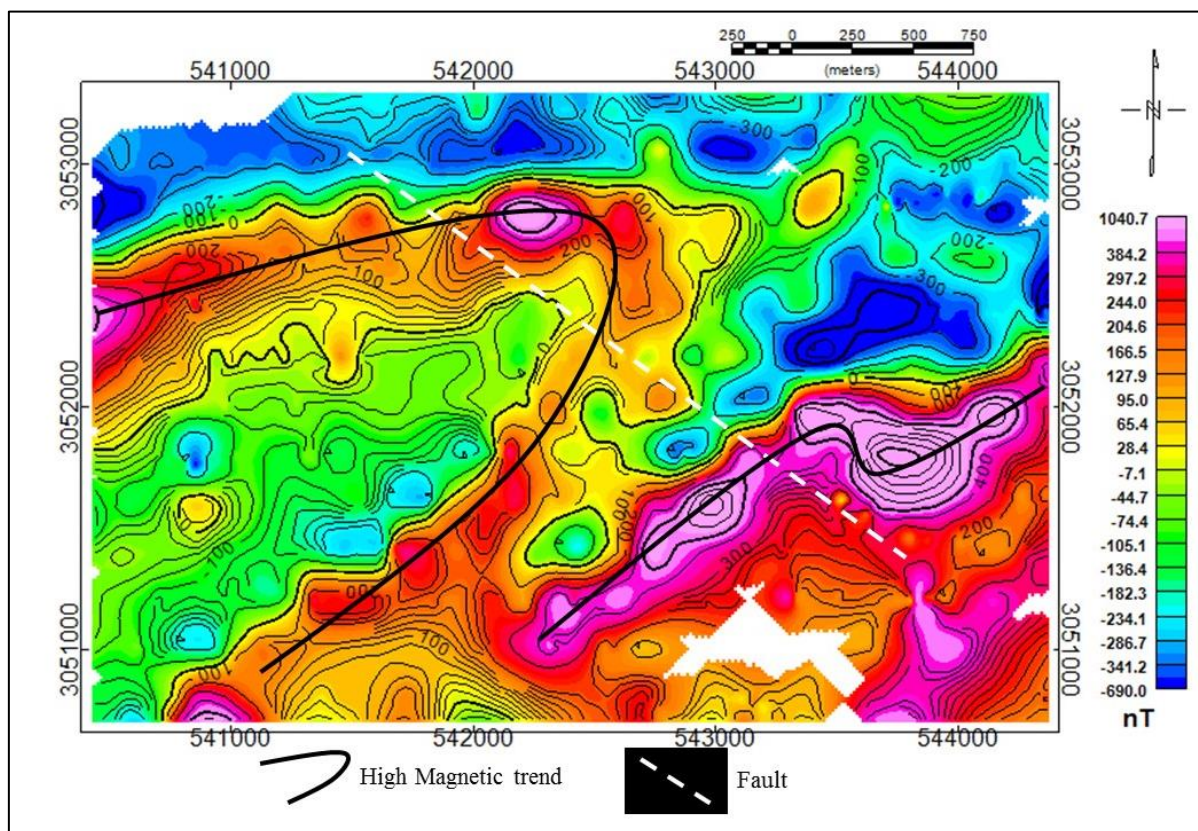


Figure 4.3. Total intensity magnetic map of Rajpura area, NE of Prithivipura, Sikar district, Rajasthan.

#### **4.5.1b. Reduced to pole (RTP) anomaly map**

Magnetic data are transformed into wave number domain using Geosoft software for further processing and enhancement of the magnetic data. To remove the inclination ( $43.46^0$ ) and declination ( $1.15^0$ ) effect and to make the interpretation easier, reduced to the pole (RTP) filter has been applied on total magnetic anomaly grid and RTP image generated (Figure 4.4).

From the analysis of RTP image, a high magnetic ( $>1000\text{nT}$ ) anomaly trending NE-SW direction has been observed towards north of Rajpura. The shape of the magnetic anomaly appears to be folded structure under soil cover. The causative source of high magnetic folded feature may be due to quartzite bearing magnetic minerals like magnetite/pyrrhotite in quartzite. A small quartzite ridge exposure as marked polygon in figure 4.4, was characterized by high magnetic anomaly as a part of fold. The eastern limb of the fold appears to be overturned as per magnetic signatures. A low magnetic zone ( $-100$  to  $-300\text{nT}$ ) trending NE-SW direction (marked as solid white line in figure 4.5) was observed along the fold axis which may indicate altered zone or Quartz-Biotite-Schist devoid of magnetic minerals. Magnetite bearing quartzite and QBS are folded together with QBS in the core of the fold or axis, the magnetic response of magnetite bearing quartzite clearly define the folding in the area. RTP response peaks over the magnetic source defines well the folded structure in the area compared to TMI anomaly map.

To the north of Fathepura, another high magnetic anomaly in folded pattern trending NE-SW direction is identified under soil cover. Low magnetic anomalies towards northern most part of the map represent sheared quartzite.

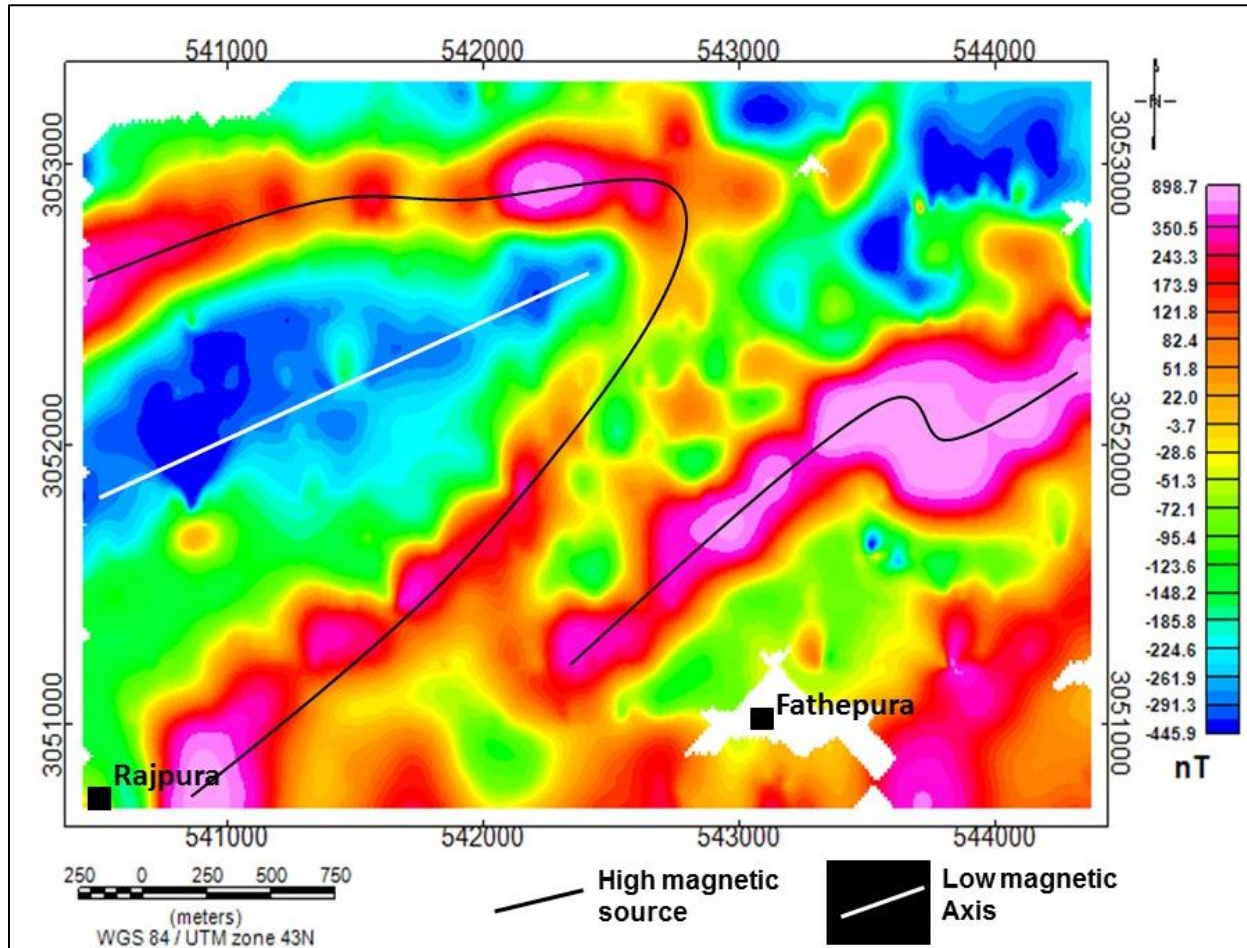


Figure 4.4. Reduced to pole (RTP) map of Rajpura area, NE of Prithivipura, Sikar district, Rajasthan.

#### 4.5.1c. First vertical derivative map

In order to enhance the shallow features and to resolve the closely spaced magnetic bodies, multiple filters i.e. first vertical derivative and upward continuation (30m, to suppress the accentuated shallow surface noise due to the first derivative filter) have been applied to magnetic data (RTP). Final derivative filtered image (Figure 4.5) has clearly brought out high magnetic folded structures in the study area by resolving the fold limbs. Low magnetic zone along fold axis near Fathepura can also be seen in derivative image which was not clearly visible in the RTP image. Three faults have been delineated in NW-SE direction based on offset of anomalies.

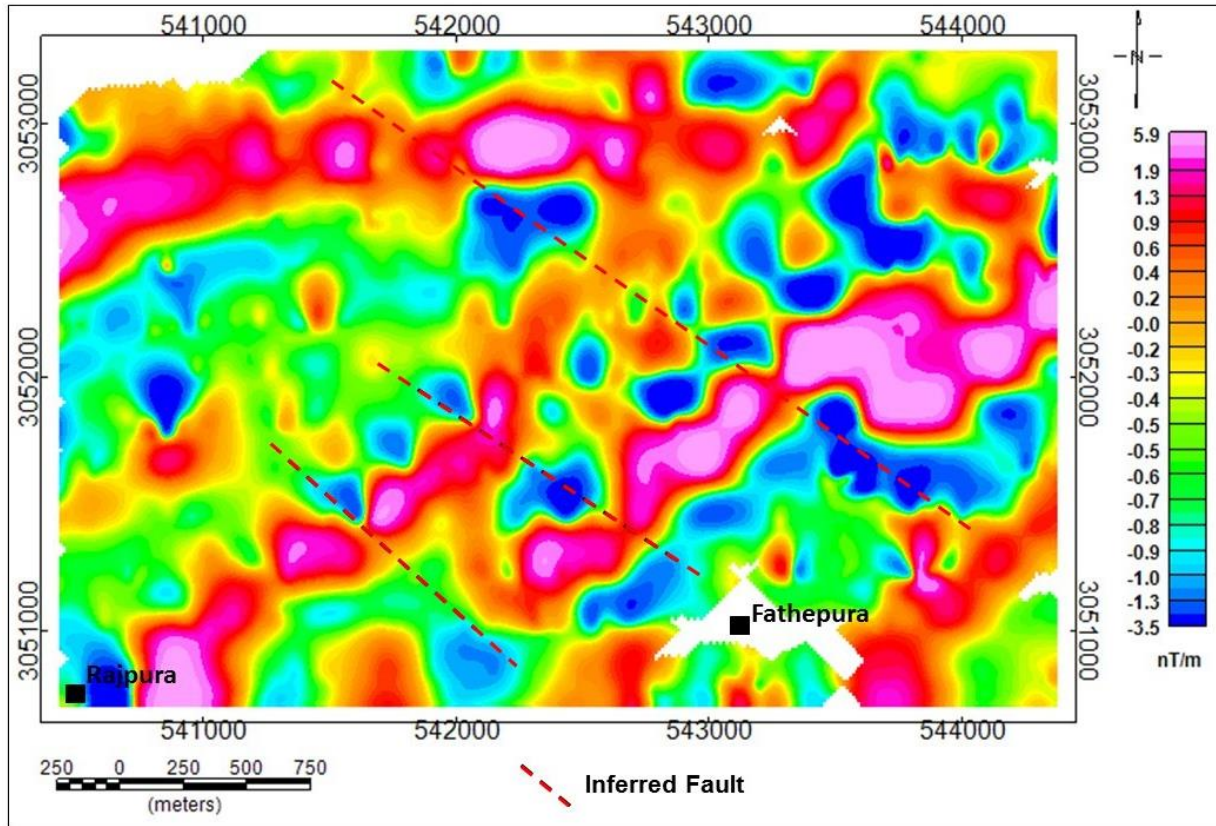


Figure 4.5. First vertical derivative (30 m Upward continued) map of Rajpura area, NE of Prithivipura, Sikar district, Rajasthan.

#### 4.5.2 Quantitative interpretation

Quantitative interpretation refers to the quantification of the magnetic anomalies or getting the source parameters such as depth, dimension, geometry, spatial location etc. Various quantitative interpretation methods are used for the estimation of the above parameters. Methods like Euler deconvolution and forward modeling are generally used for the quantitative analysis of the magnetic data. Inversion of data is yet another efficient method for the purpose. The detailed explanation of the methods used is described below.

#### 4.5.2a. Euler Deconvolution

The earlier methods of depth estimation are best suited for anomalies caused by single, isolated sources. Another class of techniques uses a different strategy, namely, to consider magnetic anomalies to be caused by many relatively simple sources. Such a strategy is amenable for long profiles or large surveys with many anomalies. For example, a technique that can estimate the location of a simple body from only a few measurements of the magnetic field could be applied to a long profile of measurements by dividing the profile into windows of consecutive measurements, each window providing a single estimate of source location. When all such determinations are plotted in cross section, they tend to cluster around magnetization contrasts of geologic interest. Euler's equation leads to one such method. Euler's equation in its general form is given by-

$$\mathbf{r} \cdot \nabla f = -nf \quad \text{Eq. (4.3)}$$

Where,  $\mathbf{r}$  is the position vector,  $f$ : function of spatial coordinates and  $n$ : structural index or attenuation rate.

Functions  $f$  that satisfy Euler's equation are said to be homogeneous; if they also satisfy Laplace's equation; they can be represented in spherical coordinates as a sum of spherical surface harmonics. Any spatial derivative of a homogeneous function is also homogeneous.

If  $\Delta T_i$  be the  $i^{th}$  point of a magnetic survey over a simple body, such as a sphere or cylinder, with the point of measurement at  $(x, y, z)$ , and the centre of the body at  $(x_0, y_0, z_0)$ .

Eq. (4.4) can be solved for the position of the source  $(x_0, y_0, z_0)$  and structural index ( $n$ ). Since there are four unknowns and 'n' equations, where  $n > 4$ , hence the solutions are non-unique. (Blakely, 1995). Figure 4.6 shows the Euler depth solutions for the magnetic data for structural index 1.0.

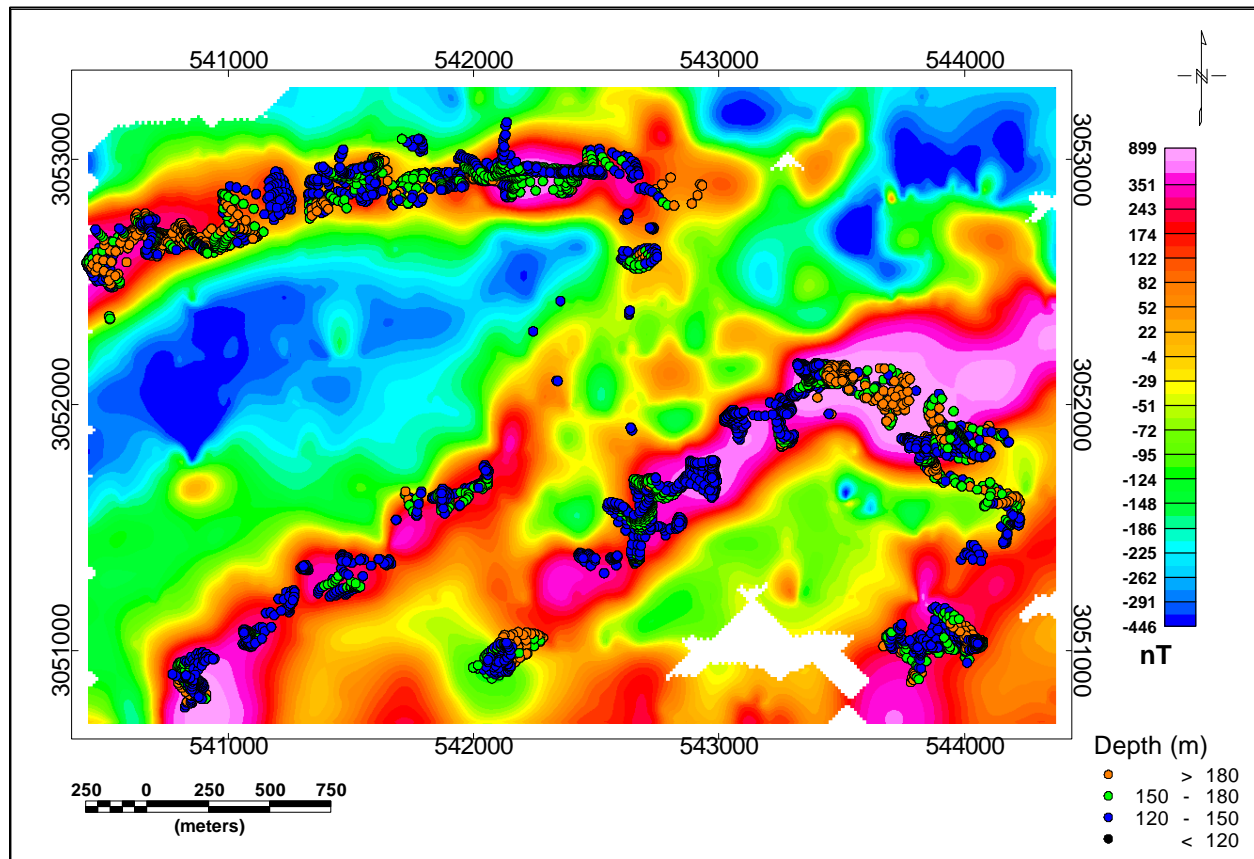


Figure 4.6. Euler depth solutions for magnetic data from Rajpura area, NE of Prithivipura, Sikar district, Rajasthan.

The Euler depth solutions plotted with structural index 1.0 depict the location and the depth of the source pertaining to dyke/sill (plate). The fold limbs can be best considered to be that of dipping sheet/plate, hence structural index was chosen to be 1.0. The depth solutions reveal the general depth to the top of the folded structure to be between 120-150m. Towards the western side higher depth is encountered, greater than 180m. These results are used in determining the bounds for the depth range in the inversion algorithm.

#### 4.5.2b. Forward modeling of magnetic data

Forward modeling is a process of getting data from the model. Simple geometric shapes such as sphere, horizontal cylinder, vertical cylinder, thin sheet, slab etc. are selected and the

mathematical formulation is developed to compute the magnetic anomaly from these shapes at different latitudes, inclination and susceptibility value. Forward modeling is used in quantitative interpretation (Chapter-6) as the computed anomaly that closely resembles the observed anomaly may be an indicative of the source parameters. A thin sheet model is shown in Figure 4.7, that was generated in MAGFORWARD program developed in PYTHON environment. The model shown in figure 4.8 has been generated with the source parameters as listed below-

Source shape: Thin Sheet

K (Amplitude coefficient): 1000 nT

$\Theta$  (Index angle):  $-24^\circ$

S (Structural index): 1.0

$X_0$ (Source location): 0 m

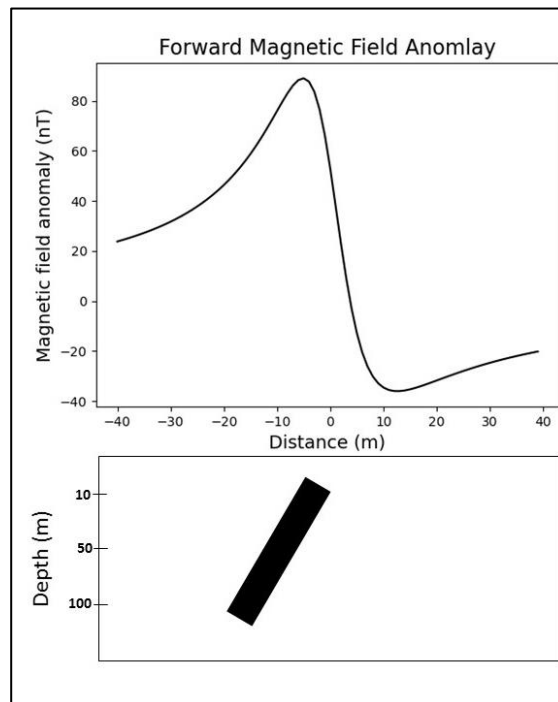


Figure 4.7. Predicted anomaly of a thin sheet like structure. Anomaly computed using MAGFORWARD program in PYTHON programming language.

#### 4.5.2c. Inversion of magnetic data

Inversion/ Inverse modeling is the use of the actual results of some measurements of the observable parameters to infer the actual values of the model parameters (Tarantola, 2005). The distinction between the forward modeling and inversion can be visualised using the simple flow structure of the two methods as shown in Figure 4.8 and Figure 4.9 respectively.

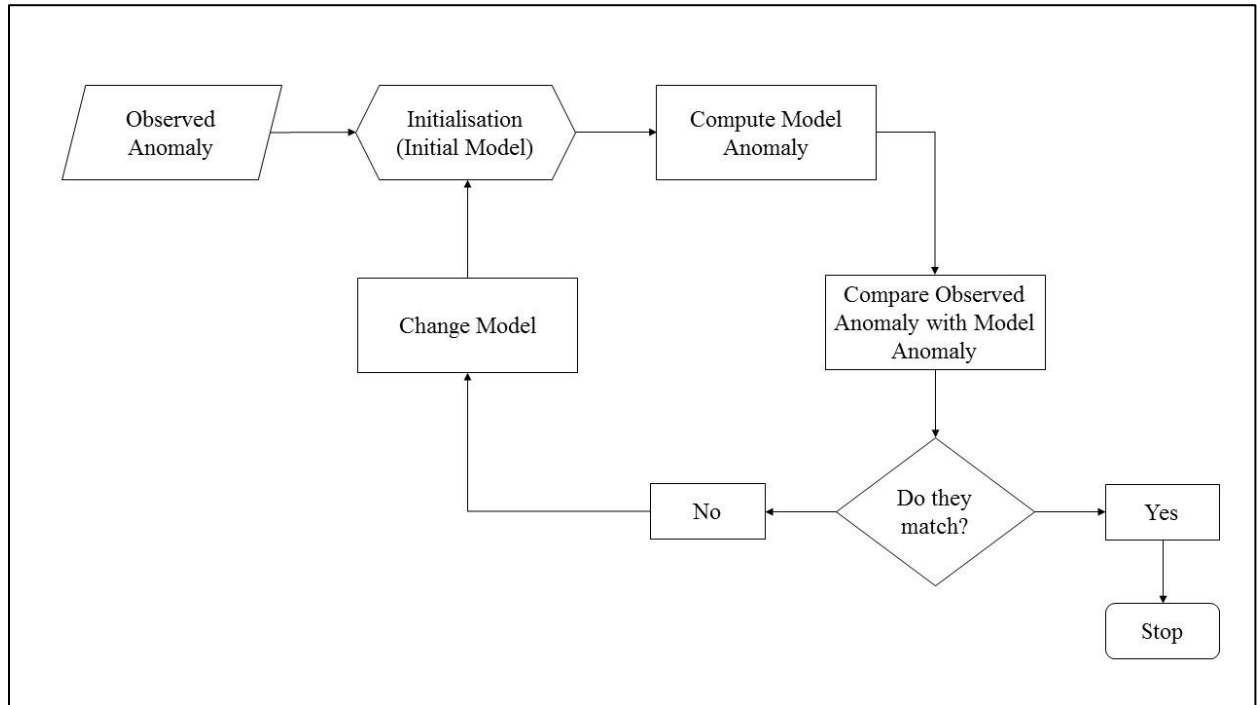


Figure 4.8. Flow Structure of forward modeling.

The role of inverse theory is to provide information about unknown numerical parameters that go into the model, not to provide the model itself. The starting place in most inverse problems is a description of the data.

If  $N$  measurements are performed in a particular experiment, for instance, then these numbers can be considered the elements of a vector  $\mathbf{d}$  of length  $N$ . Similarly, the model parameters can be represented as the elements of a vector  $\mathbf{m}$ , which, is of length  $M$ .

$$\text{data: } \mathbf{d} = [d_1, d_2, d_3, \dots \dots \dots d_N]^T \quad \text{Eq. (4.4)}$$

$$\text{model parameters: } \mathbf{m} = [m_1, m_2, m_3, \dots \dots \dots m_M]^T \quad \text{Eq. (4.5)}$$

where,  $T$  is for matrix transpose.

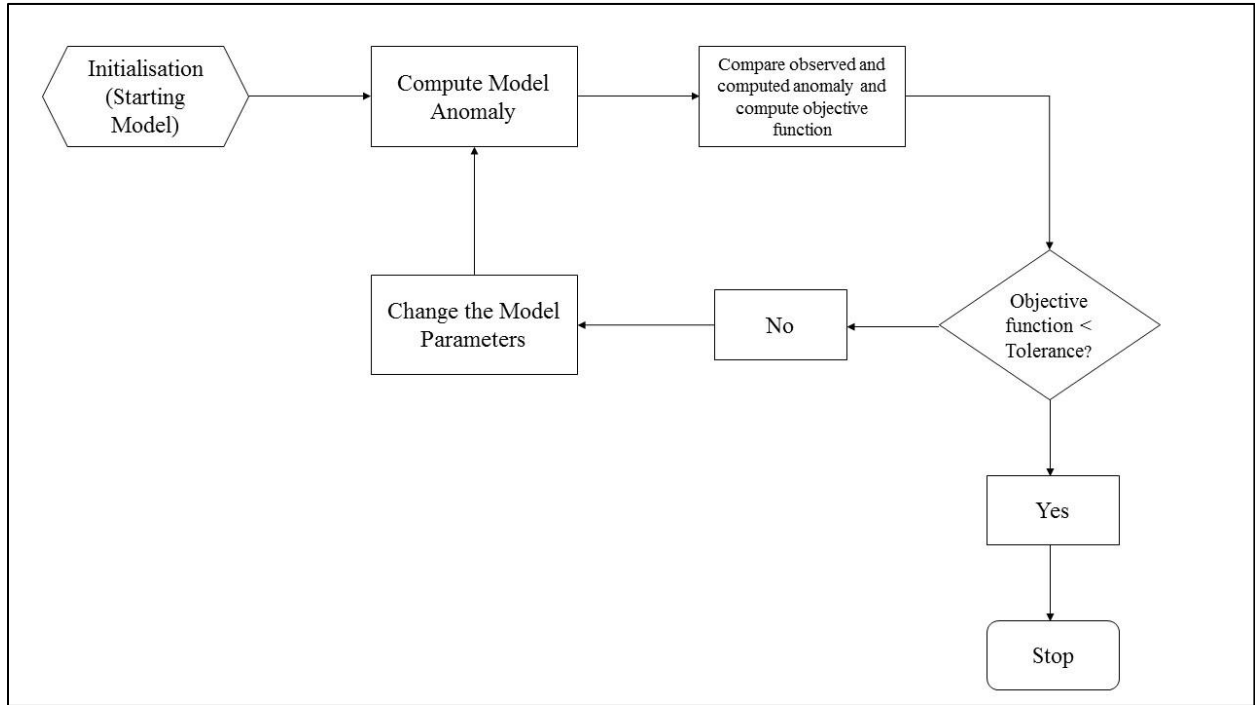


Figure 4.9. Flow Structure of inverse modeling/ inversion.

The process of inversion tends to find a mathematical relation between the observed data and the model parameters, called the *Model*. This is achieved through a process of error minimization or called as the cost function optimisation. The cost function is nothing but the error function between the observed data and the predicted data (Menke, 1984).

Inversion schemes are broadly divided into two types based on the type of relationship between the model parameters and the data-

- i) Linear inversion schemes (Linear relationship,  $\mathbf{G} \cdot \mathbf{m} = \mathbf{d}$ ),  $\mathbf{G}$  is the kernel matrix
- ii) Non-linear inversion schemes

They can also be classified based on the optimum solution that the scheme seeks-

- i) Local optimisation (Newtons method, Conjugate gradient, Non-linear conjugate gradient, Least squared, etc.)

- ii) Global optimisation (Monte-Carlo, Simulated annealing, Particle swarm optimisation, Grey wolf optimisation, etc.)

There are a number of optimisation schemes which can be used for the inversion of data. It depends on the type, complexity and dimension of the problem so as which inversion scheme to be chosen.

From the magnetic survey, the sub-surface structural features were demarcated along with the weak zones (fractures/faults), which can act as conduits for the flow of fluid. The attributes of the prominent structural feature in the area were estimated using the quantitative interpretation methods. IP/Resistivity survey was taken up to look for disseminated sulphide minerals that are favourable for precipitation of U-mineralisation due to the reducing environment they offer.

## CHAPTER-5

### IP/RESISTIVITY SURVEY

#### 5.1 IP/Resistivity data acquisition

IP/Resistivity data were acquired over an area of 5sq. km by employing gradient array in order to scan the area for high chargeability zones in minimum time, with an average traverse length of  $\sim 3$  km using IRIS IP (VIP 5000) ([http://www.iris-instruments.com/Pdf_file/Vip_5000.pdf](http://www.iris-instruments.com/Pdf_file/Vip_5000.pdf)) instrument. IP/Resistivity survey were planned initially in the magnetic lows, since those were the areas where weak zones prevail. Apparent chargeability and resistivity parameter were recorded along the traverses. Chargeability decay curve was recorded in 20-time gates in the arithmetic mode. The arithmetic mode divides the time gates into equal time interval of 80 ms each. The survey was carried out with a line spacing of 200 m and station interval of 50 m. Later in the regions of high chargeability, pseudo depth section data were acquired employing dipole-dipole array to know the depth persistency of the zones. For pseudo depth section, data up to 6 levels ( $n = 1$  to 6) were recorded. The IP/Resistivity survey layout and traverse lines are shown in Figure 5.1. The black dots show the IP/Resistivity stations.

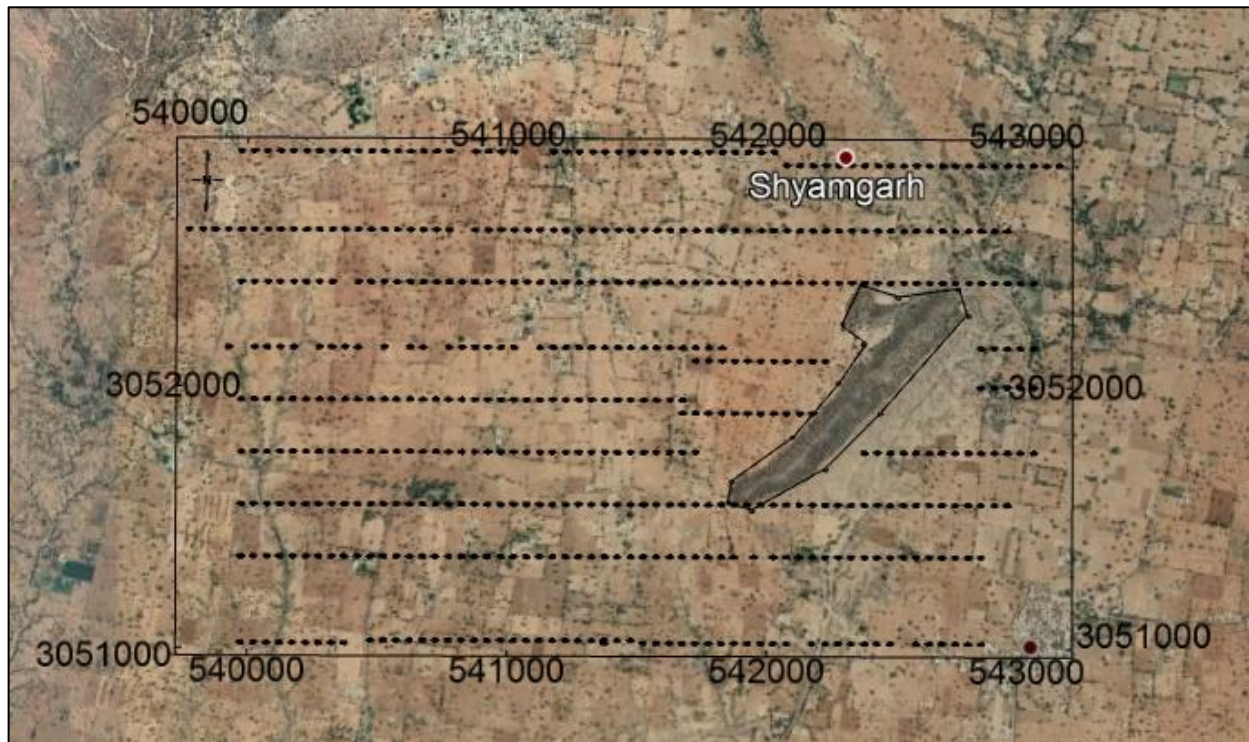


Figure 5.1. IP/Resistivity survey station locations in Rajpura area, NE of Prithivipura, Sikar district, Rajasthan.

## 5.2 Principle of IP/Resistivity measurement

The technique used to measure induced polarization is similar in many ways to those employed for resistivity measurements. Current is introduced into the earth with two electrodes, and a potential is measured across the other two electrodes after the current is shut off (Time domain IP) (Dobrin and Savit, 1988). The ratio of the voltage output to the current input is called the resistance of the earth (Hohmann and Ward, 1981). During on-time, the current values are recorded from the transmitter and the voltage values are recorded from the IRIS receiver and their ratio ( $V/I$ ) on multiplying with the geometrical factor 'K' of the array system gives the resistivity value of the subsurface earth. The sub-surface distribution of electrical conductivity/resistivity and chargeability is interpreted in terms of geology. Here the impedance is measured in time domain, where the current is periodically turned on and off. As the induced

polarization used the variation of resistivity with frequency, it is the reason why an alternating current is used (Bhattacharya and Shalivahan, 2016). Figure 5.2 shows the transmitted and received waveforms in time domain measurement.

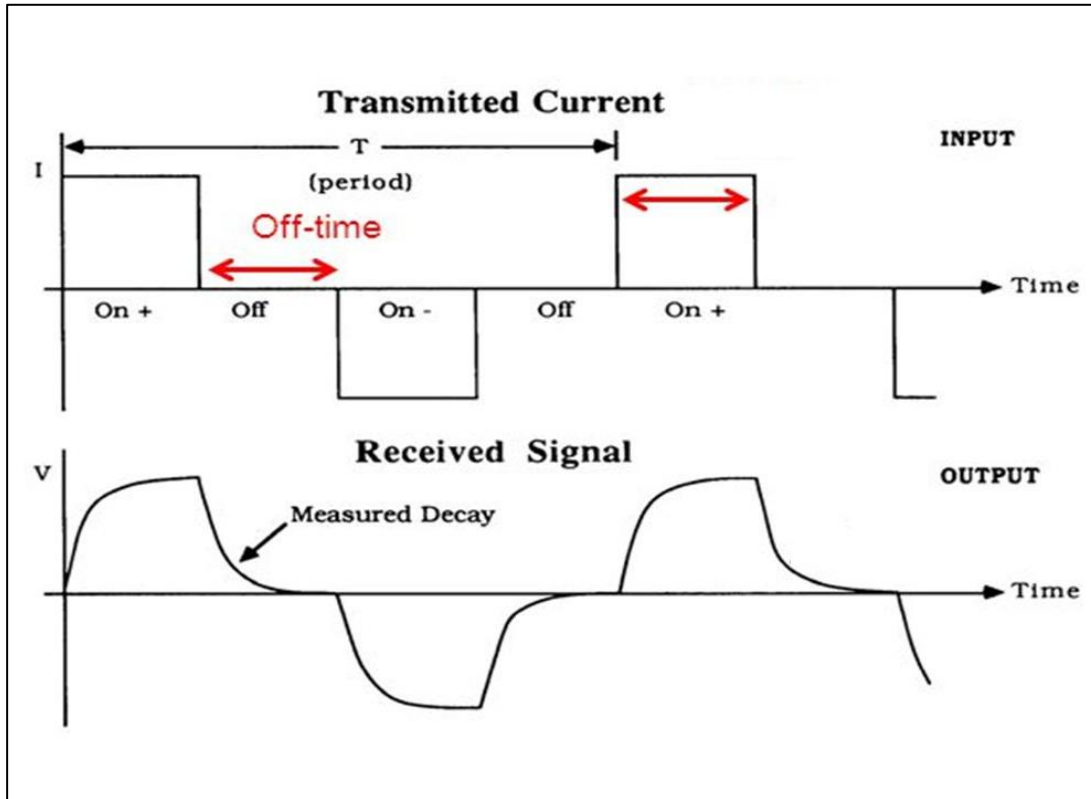


Figure 5.2. Transmitted and received waveforms in time domain IP survey. ( $V_p$  is the primary voltage).

### 5.2.1 Time-domain measurements

Time domain IP measurements can be done in the following ways, millivolt per volt, it is the ratio of the voltage  $V_t$  at a time  $t$  after the current is cut-off with the steady voltage  $V_p$  (primary voltage) during the current flow interval having a unit of mV/V or IP percent. In all time domain measurements, there is a large transient caused by cutting off the current circuit, hence it is not possible to measure the potential at the instant of current cut-off and also  $V_t$  must be measured before the residual voltage has decayed to noise level.

The decay time integral, measures potential integrated over a definite interval of the transient decay. If the integration time is short and if the decay curve is sampled at several points, then the values of the integral are a measure of the potential existing at different times. The most used TDIP measurement is the chargeability, which is the area of the decay curve between two-time intervals normalized with the primary voltage after the current is cut-off (Bhattacharya and Shalivahan, 2016). In the present study chargeability has been recorded.

### **5.3 IP/Resistivity data presentation**

The IP/Resistivity data thus acquired is represented as decay curve for individual station or a single channel (Time-gate) from all the stations in the area may be gridded to generate the chargeability map of the area. Here, the chargeability map generated from the global chargeability (Full decay curve integration) is used for processing and interpretation. The data have been gridded using minimum curvature gridding algorithm with a grid cell size of 50 m in Geosoft software of Oasis Montaj. Figure 5.3 shows a characteristic decay curve at a particular station for 20 channels for two sends off time, from the field data from Rajpura area, NE of Prithivipura, Sikar district, Rajasthan.

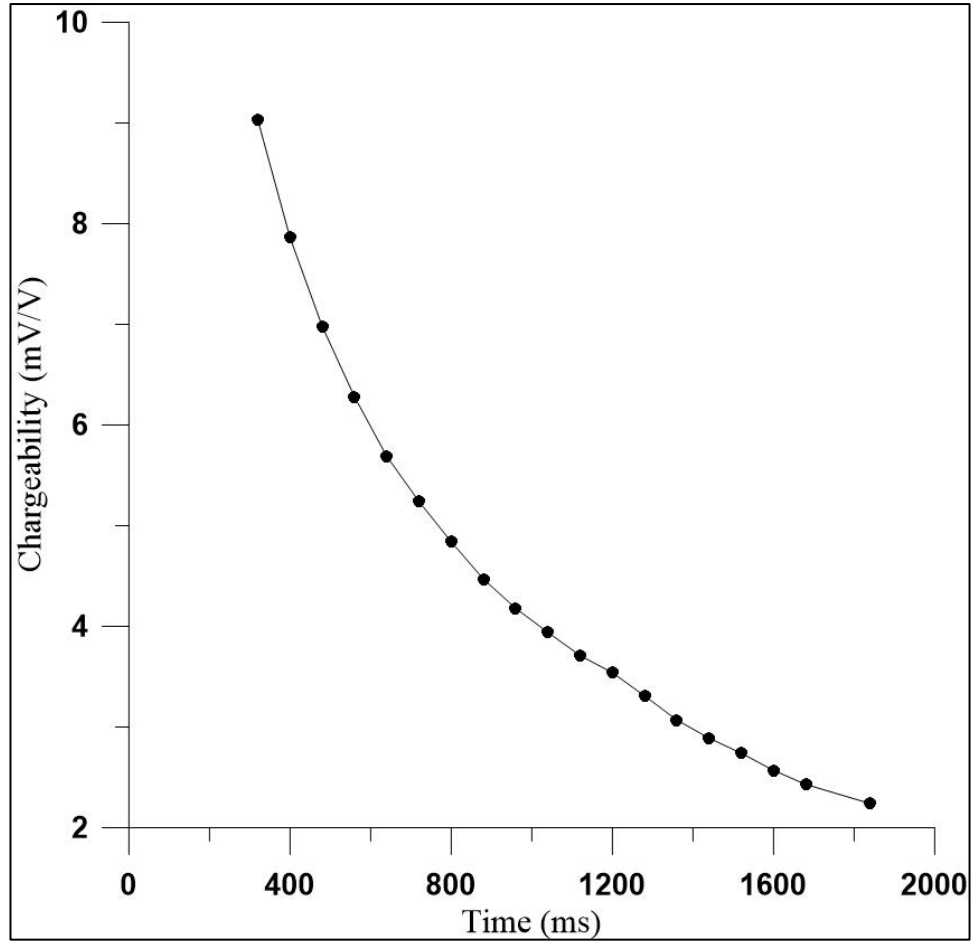


Figure 5.3. Decay curve response (one station) of Induced polarization data, from Rajpura area, NE of Prithivipura, Sikar district, Rajasthan.

#### 5.4 Processing of IP/Resistivity data

In principle, the measured data sets during the IP/resistivity survey are the bulk resistivity and global chargeability (contrast to Newmont chargeability the integration is carried from 0.15 to 1.1 seconds after the current is cut-off, Van Voorhis et. al., 1973) of the subsurface, which is also known as apparent resistivity and apparent chargeability respectively. After the data acquisition, the measured apparent resistivity and chargeability data were downloaded from the memory of the IRIS instrument using the ProsysII software for further processing and analysis. In the initial stage of processing, automatic filtering technique was used for the elimination of

random noise. The resistivity data were checked station wise to remove any near surface effect prevailing in the data. The pseudo-depth data were inverted using the RES2DINV software to bring out the subsurface resistivity and chargeability distribution., to aid in interpretation.

## **5.5 Interpretation of IP/Resistivity data**

IP/resistivity data interpretation involves the description of the chargeability zones and the resistivity distribution of the subsurface in terms of geological domains.

### **5.5.1 Qualitative Interpretation**

#### **5.5.1a. Apparent resistivity map**

Figure 5.4 shows resistivity image of the study area with resistivity values in the range of 30-600 Ohm-m. High resistivity values of the order 350-600 Ohm-m in the study area are due to Quartzite. The moderate to low resistivity values of the order of 40 – 200 Ohm-m are attributed to the quartz-biotite-schist rocks. Chargeability zones superimposed over resistivity image indicate that high chargeability is correlated with low to moderate resistivity values (30-250 Ohm-m) indicating presence of conducting minerals in host rock. Faults have been delineated trending NW-SE direction based on offset of resistivity zones.

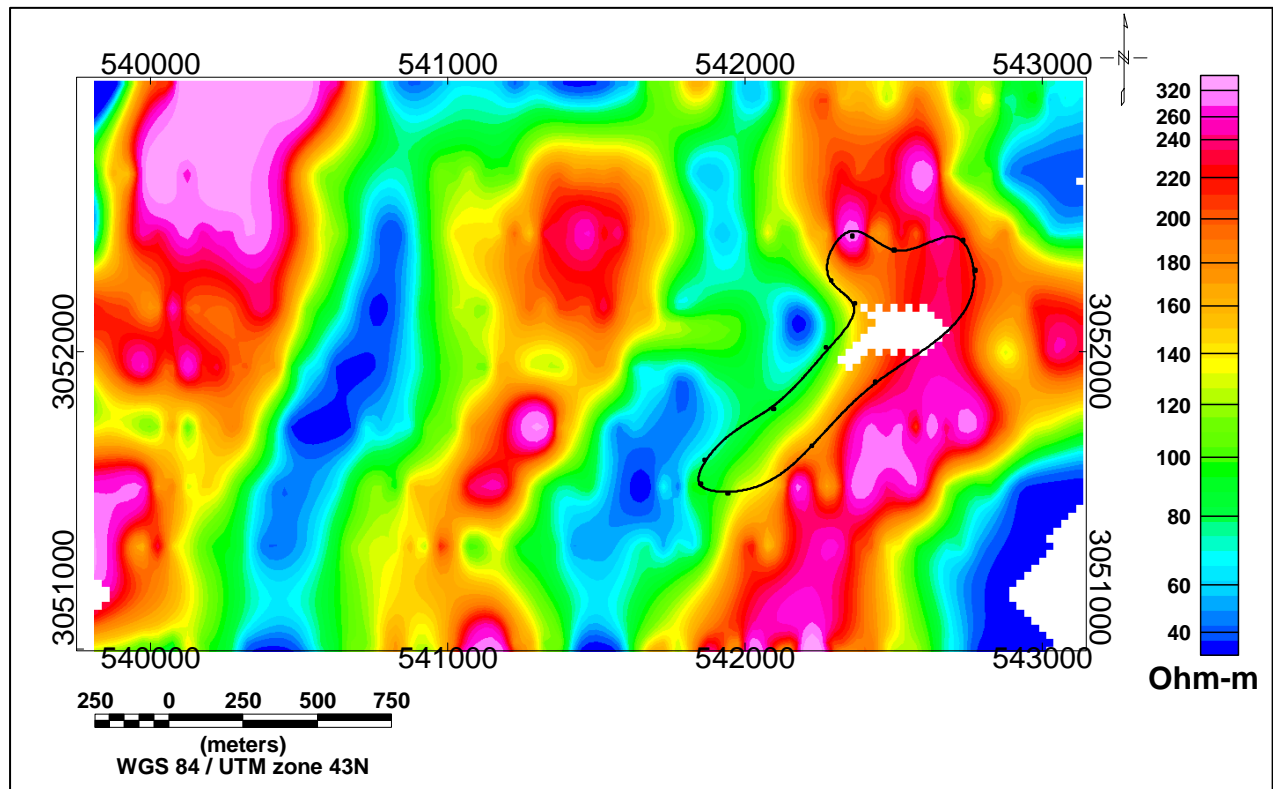


Figure 5.4. Apparent resistivity map of the study area. (NE-SW trending high resistivity zone in the SE close to the exposed quartzite ridge, this confirms that the ridge is dipping SE and at depth below the soil cover).

#### 5.5.1b. Apparent chargeability map

IP/Resistivity survey has brought out three high chargeability zones trending NNE-SSW to N-S direction under soil cover as shown in Figure 5.5. The chargeability value varies from 10-27 mV/V. The width of the chargeability zones is around 500 m with a strike length of 1.5-2 km. The causative source of chargeability zones could be due to disseminated sulphide minerals such as pyrite, chalcopyrite and pyrrhotite in Quartz Biotite Schist/Quartzite. No significant chargeability anomalies are observed towards the western side.

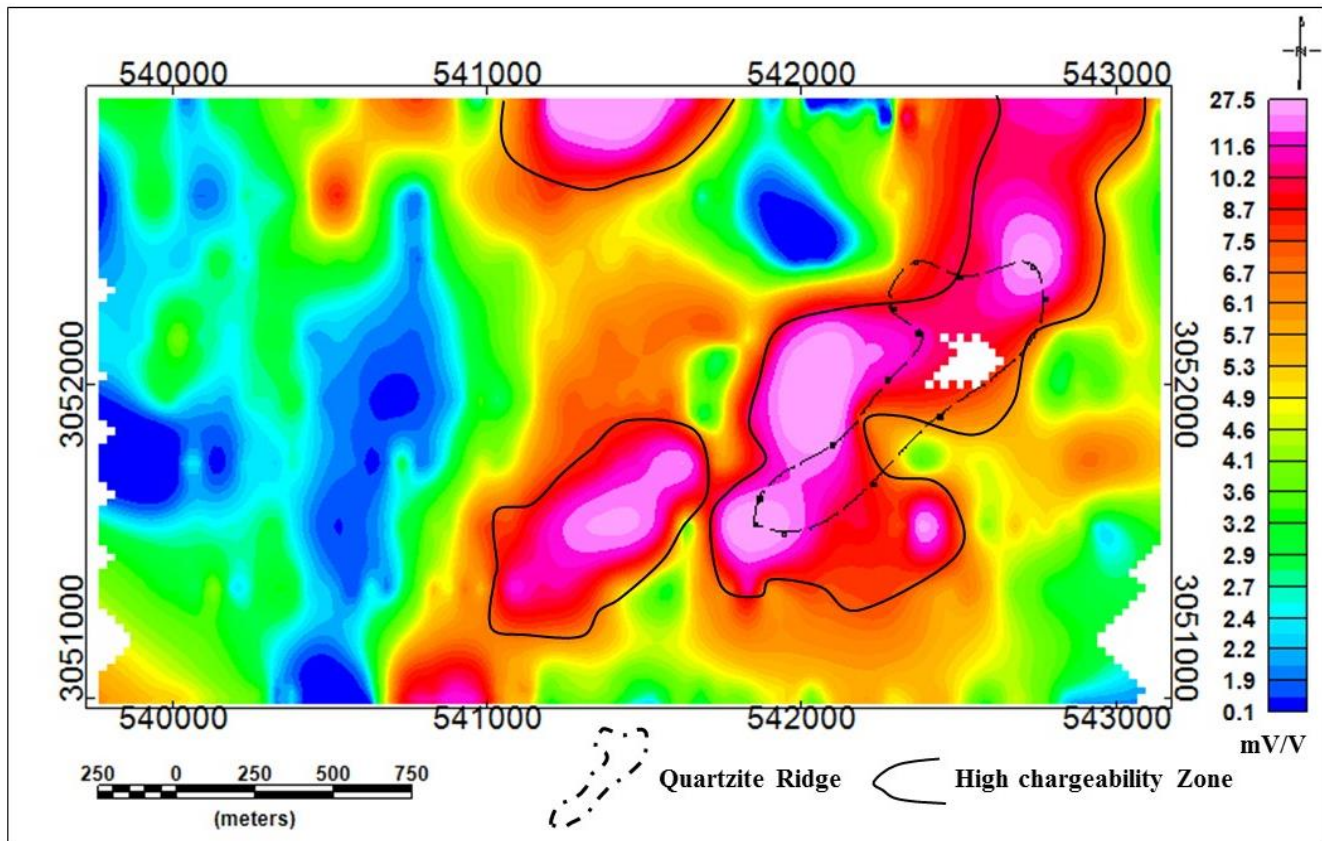


Figure 5.5. Chargeability map of Rajpura area, Sikar district, Rajasthan.

## 5.5.2 Quantitative Interpretation

### 5.5.2a. Inversion of Pseudo-depth section data

The pseudo depth section data gives depth information in levels (n), as the current electrodes and potential electrode separation increases by integer factors times the separation between the current electrodes. The inversion of pseudo-depth section has been carried out to know the depth persistency of the high chargeability zones. The inversion was carried out using RES2DINV[®] software (Loke, 2019). The inversion is carried out starting with a forward modeling subroutine to calculate the apparent resistivity values, and a non-linear least squares optimisation technique is used for the inversion routine. (Loke, 2019).

The inverted depth section depicts the depth persistency of the chargeability zones and the resistivity distribution of the subsurface with depth. The two sections are used for correlation between the chargeability and the resistivity. Figure 5.6 shows the inverted depth sections of the IP/resistivity data.

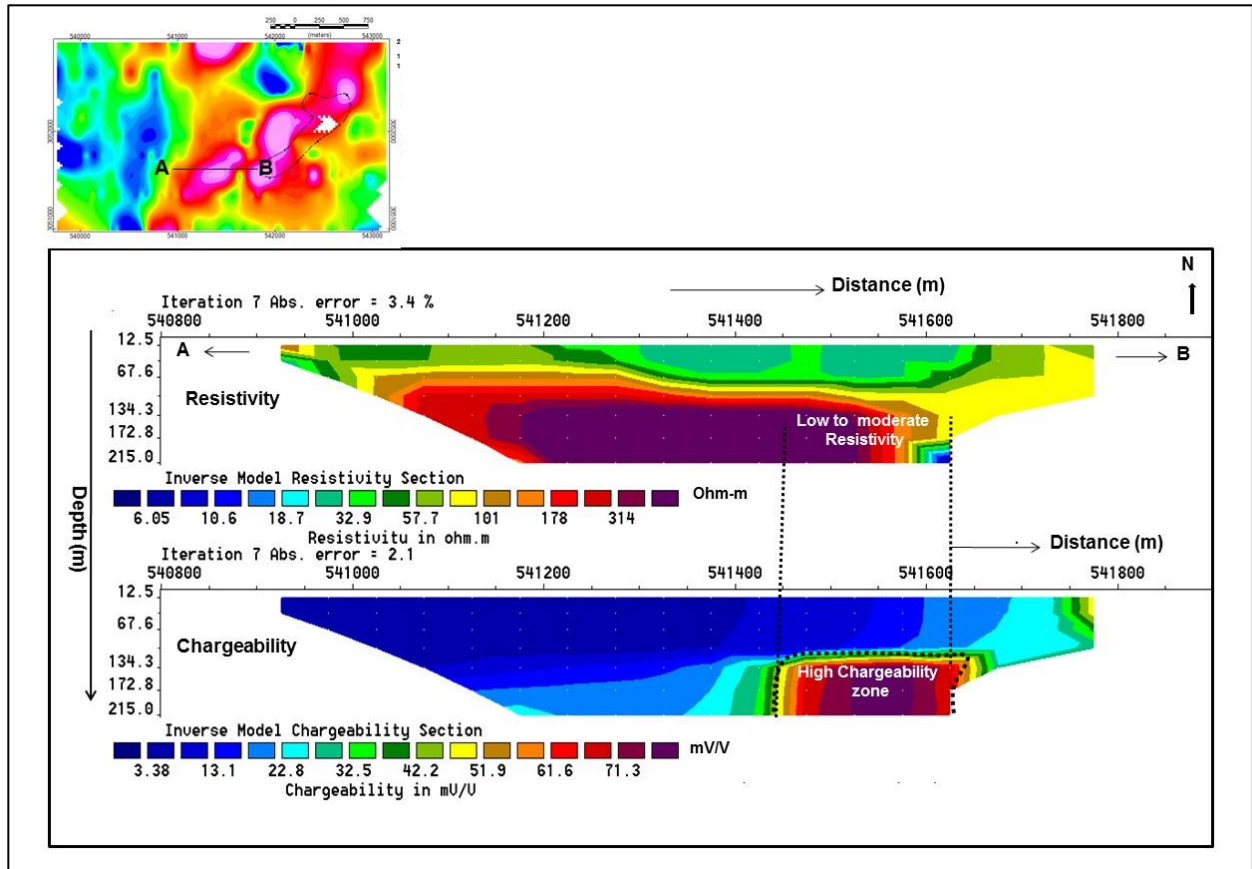


Figure 5.6. Inverted depth sections of IP/Resistivity data. (Resistivity (Top) and Chargeability (Bottom)).

Figure 5.6, which shows inverted depth section of resistivity (top) and chargeability (bottom) along AB line with the maximum depth of investigation obtained is up to 215m depth. Inverted depth section indicates, significant chargeability zone (30-70 mV/V) (marked as black dotted curves) occurring at a depth of 110 m towards eastern side. The amplitude and width of the chargeability zone increases up to 215m depth and persists with increasing depth. In

resistivity depth section, very low resistivity values of the order of <70 Ohm-m up to 60m depth indicates the effect of overburden, which can also be observed from the magnetic data modeling (Figure-7.1). The correlation of high chargeability zone with low to moderate resistivity values of the order of 70-300 Ohm-m indicates the occurrence of disseminated sulphide minerals along fractured/sheared contact of the QBS and Quartzite. The high resistivity values of the order >300 Ohm-m at the central portion represent quartzite.

### 5.5.2b. IP decay curve analysis

An attempt was made to have an idea about the mineral type and volume using the IP decay curve analysis (Pelton, et al. 1978). The decay curve analysis was carried out using the DECAY_ANALYSIS program developed in Python 3.6. The program was used to fit a decaying double exponential curve to the observed data and return the time constants  $\lambda_1$  and  $\lambda_2$  respectively. The sum of two exponentials used for the purpose is-

$$M = Ae^{\frac{-t}{\lambda_1}} + Be^{\frac{-t}{\lambda_2}} + C \quad \text{Eq. (5.1)}$$

Where, M is the observed chargeability at time 't' and  $\lambda_1, \lambda_2$  are time constants.

Least squares optimisation method from the SciPy module in Python 3.6 was used to fit the observed data to the above equation (Eq. 5.1) and the parameters A, B, C,  $\lambda_1$  and  $\lambda_2$  (where A, B and C are coefficients and  $\lambda_1$  and  $\lambda_2$  are the relaxation times) were determined. Figure 5.7 shows a plot of fitted curve with the field observation. The program returns the relaxation time values for all the stations along a line in one run. These data were plotted against the chargeability values for each station and statistical analysis was made. The analysis was made for line 301500N with the results are shown below. The exercise was carried out; first, to study distinct

characteristic in the plot of non-chargeability zone and chargeability zones, secondly, to know the volume concentration and number types of minerals present.

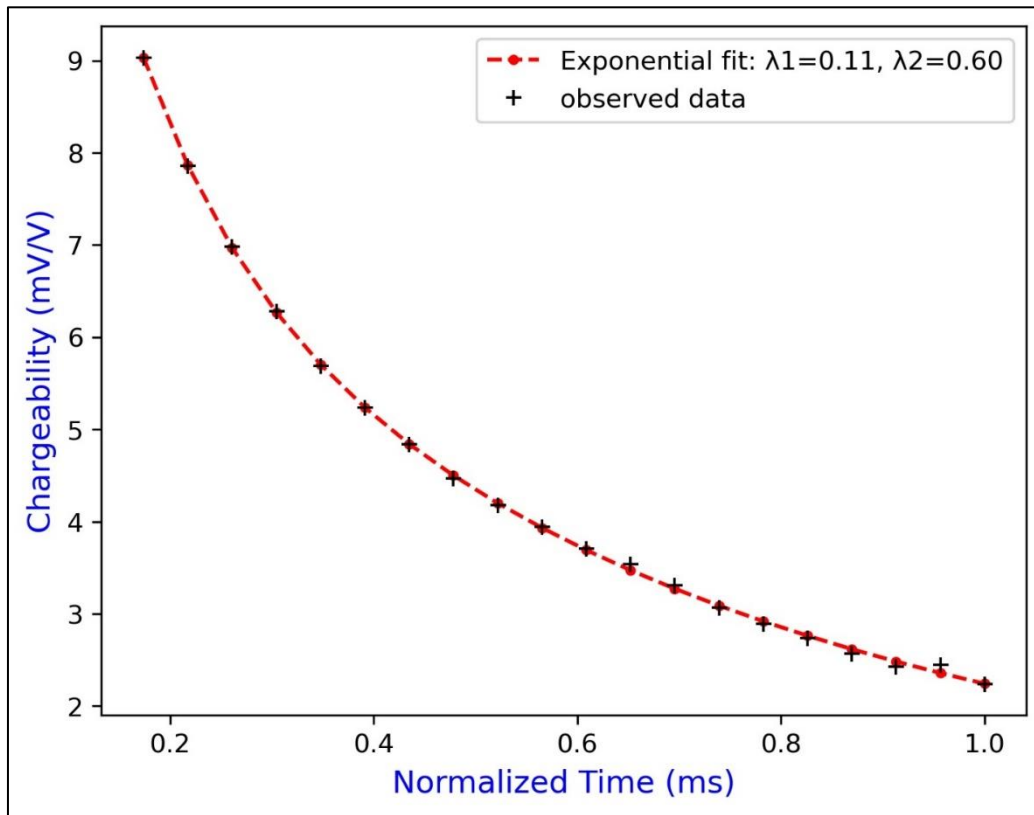


Figure 5.7. Decaying double exponential fit to observed IP field data.

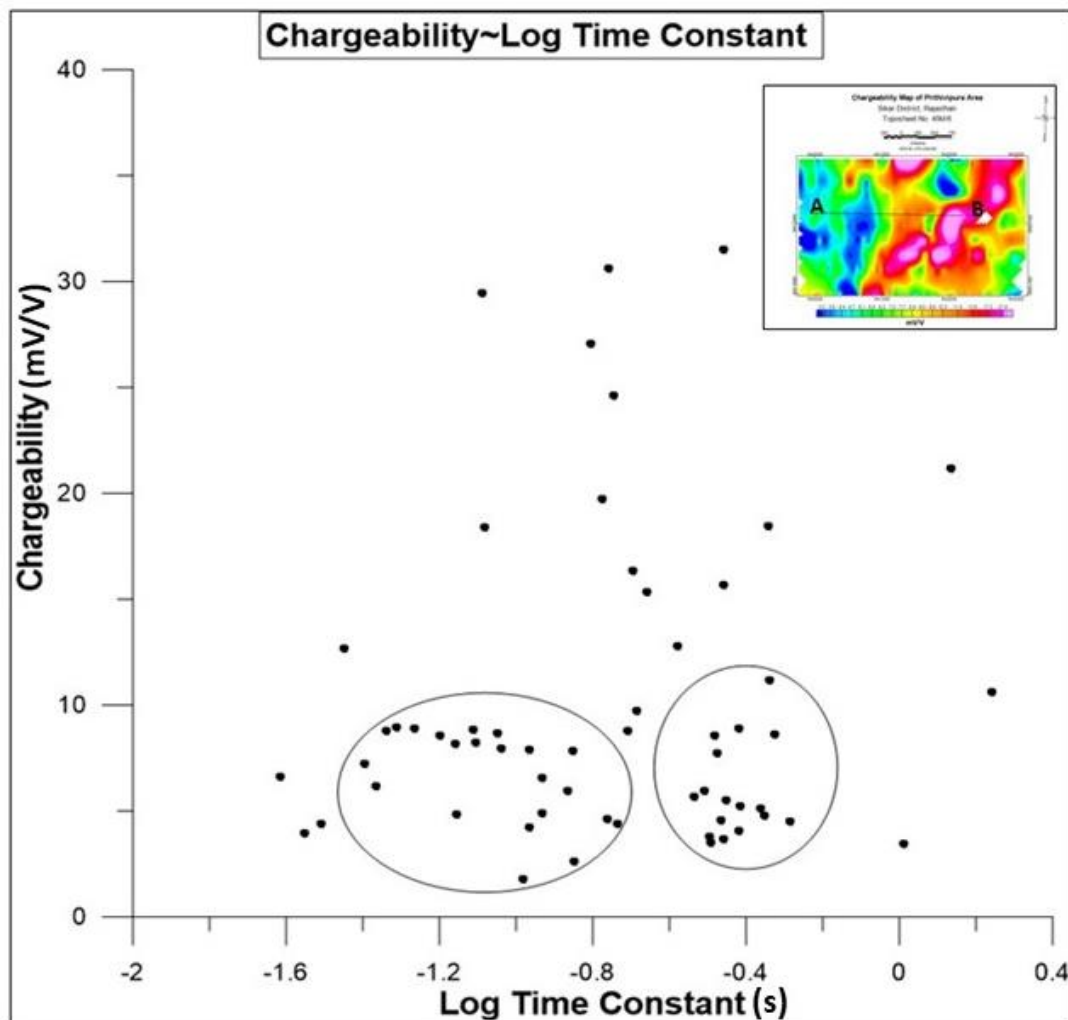


Figure 5.8: Decay curve analysis of line AB from chargeability map of Rajpura area, NE of Prithivipura, Sikar district, Rajasthan.

The above analysis suggests that both the grain size and volume of the causative mineral is increasing. The trend line analysis and correlation with the standard nomogram (Pelton, et., al. 1978) further shows that the rate of increasing volume is less than the rate of increasing concentration. Figure-5.8 shows the plot of log of time constant vs. chargeability.

# CHAPTER-6

## GLOBAL OPTIMISATION: THE PARTICLE SWARM OPTIMISATION

### 6.1 Global Optimisation approach

The modeling and inversion of the magnetic data is a quite challenging, since it is a multi-dimensional problem (more than 2 independent variables). There have been many optimisation schemes utilized in the inversion of magnetic data. The conventional schemes (Linear and non-linear) are computationally cumbersome. Hence the Particle Swarm optimisation algorithm was taken up for its ability to handle multidimensionality and also as it is computationally fast and easy to implement. Optimisation is a process of finding the solution of a set of normal equations subject to some constraints and satisfying some mathematical properties. All optimisation algorithms (linear or non-linear) can be attributed to the way of solving an inverse problem. Inversion is the process of deriving the model parameters from the data in hand. As an example, fitting some data into a straight line ( $y = m.x+c$ ) is an inverse problem, where the equation of the straight line describes all the points in hand in the 2D space. Similar example can be put forth in 3D with the symmetric equation of a line  $\frac{x}{a} = \frac{y}{b} = \frac{z}{c}$ ; a, b and c are the points through which the line passes.

The global optimisation approach finds the global best solution (minimum or maximum of all the minima or maxima) of models (linear or non-linear), Figure 6.1 shows the local and global optima of an equation. Formally, global optimisation seeks global solution(s) of an optimisation model. Nonlinear models are used in many applications, e.g., data analysis, advanced engineering design, biotechnology, environmental management, financial planning,

process control, risk management, scientific modeling, medical sciences and others. The solution of these often requires a global search algorithm.

Global optimisation algorithms are mainly applied to non-linear problems instead of linear problems (<https://mathworld.wolfram.com/GlobalOptimisation.html>), the solution of which are easy to be found using analytical methods. The formulation of global optimisation problem assumes/derives an objective function  $f$  and the number of unknowns in the set of normal equations are equal to the number of normal equations. This assumes that the problem is even-determined, such that the set of solution of the optimisation problem is non-empty and unique.

Such type of formulation of the optimisation problem is rare or many times impractical. The problems are mainly under-determined or over-determined resulting in the solution set to be non-unique.

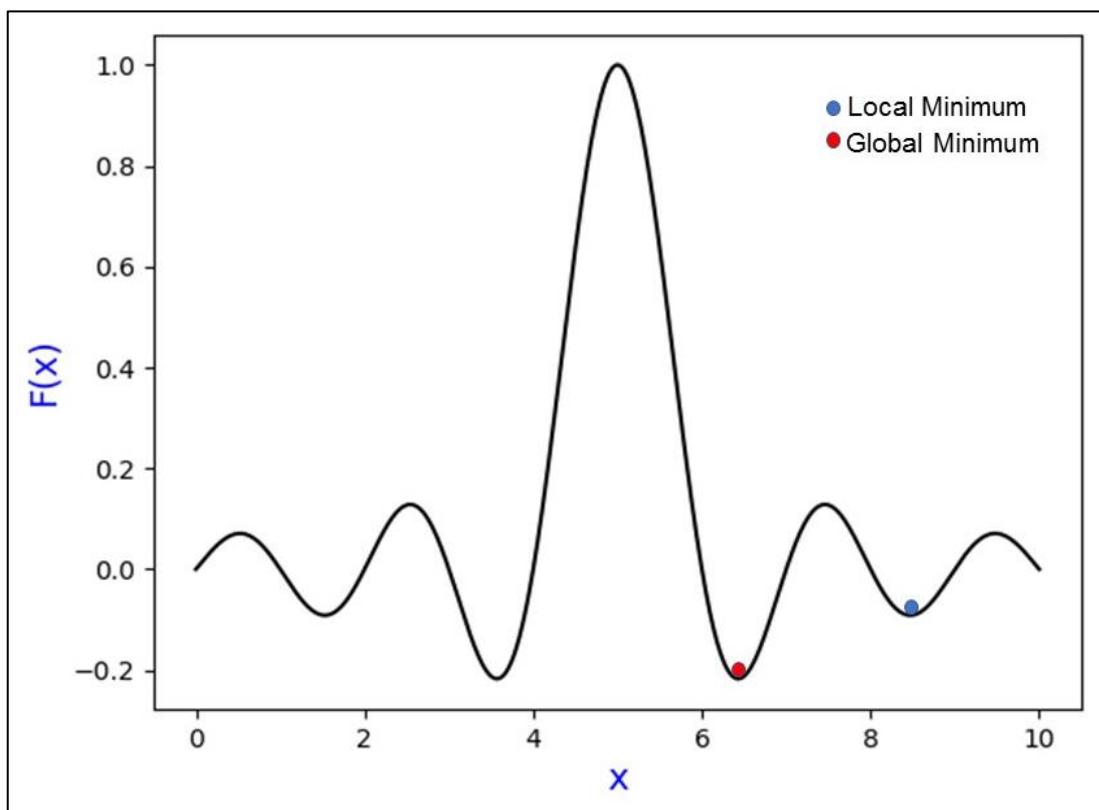


Figure 6.1. Figure showing local and global minimum of a function.

In the geophysical parlance, the problems involving the optimisation or inversion of data are multivariate and highly non-linear. Hence, an algorithm capable of handling multiple dimensions is often needed. Since the error surfaces consist of many maxima and minima hence a guided random search algorithm can be used to arrive at a global solution (maxima or minima).

Currently many search algorithms are being used widely such as, SA (Simulated annealing), VFSA (Very fast simulated annealing) (Biswas and Acharya, 2016), Monte-Carlo (Sambridge and Mosegaard, 2002), ACO (Ant colony optimisation) (Srivastava et. al., 2013), PSO (Particle Swarm optimisation, Essa and Elhussein, 2018) and also ANN (Artificial Neural Networks) (Al-Garni, 2016). The implementation of the metaheuristic or heuristic method differs from deterministic methods in the sense that heuristic methods don't use derivative (gradient) of the objective function (Kramer et. al., 2011). This gradient approach of the deterministic methods often results in the algorithm to get stuck in a local minimum. In contrary to deterministic approach heuristic methods search the complete solution space and therefore most probably arrive at the global minimum.

The above algorithms are computationally tedious and hence the PSO algorithm which is computationally relatively easier and efficient in handling the multidimensionality of the inverse problem was chosen in the present study.

### **6.1.1 Particle Swarm Optimisation**

The particle swarm optimisation (PSO), developed by Kennedy and Eberhart, is a metaheuristic search algorithm that mimics the natural behaviour of bird swarms or fish school.

In the early 1990s, studies were made regarding the natural behaviour of animals. The results showed that some animals belonging to a certain group i.e., birds and fish are capable of sharing information among the group that gives them greater survival advantage.

Inspired by the swarm intelligence, Kennedy and Eberhart proposed the PSO algorithm in 1995, a metaheuristic algorithm that can be used to optimize a non-linear continuous function. In order to understand how the natural behaviour of birds can be utilized in solving complex mathematical problems, consider a swarm of birds flying over a place to find a point to land, the point to land is analogous to the finding the optimum solution in a mathematical problem. The birds move synchronically for a period until they find the best place to land is defined and the whole flock lands at once.

The same natural behaviour of the flock is formulated mathematically and applied to the optimisation problem.

The goal of the optimisation is to determine a vector  $X = [x_1, x_2, x_3, \dots, x_n]$  that optimizes the function  $F(x)$ . Consider a swarm with ‘ $n$ ’ particles, with position of each particle represented by the position vector  $X(p)^i = (x_{i1}, x_{i2}, x_{i3}, \dots, x_{in})^T$  and a velocity vector representing the velocity as  $V(p)^i = (v_{i1}, v_{i2}, v_{i3}, \dots, v_{in})^T$  at  $i^{th}$  iteration of the  $p^{th}$  particle. These vectors are updated through the  $j$  dimensions (dimension of the problem) iteratively as per the following equation:

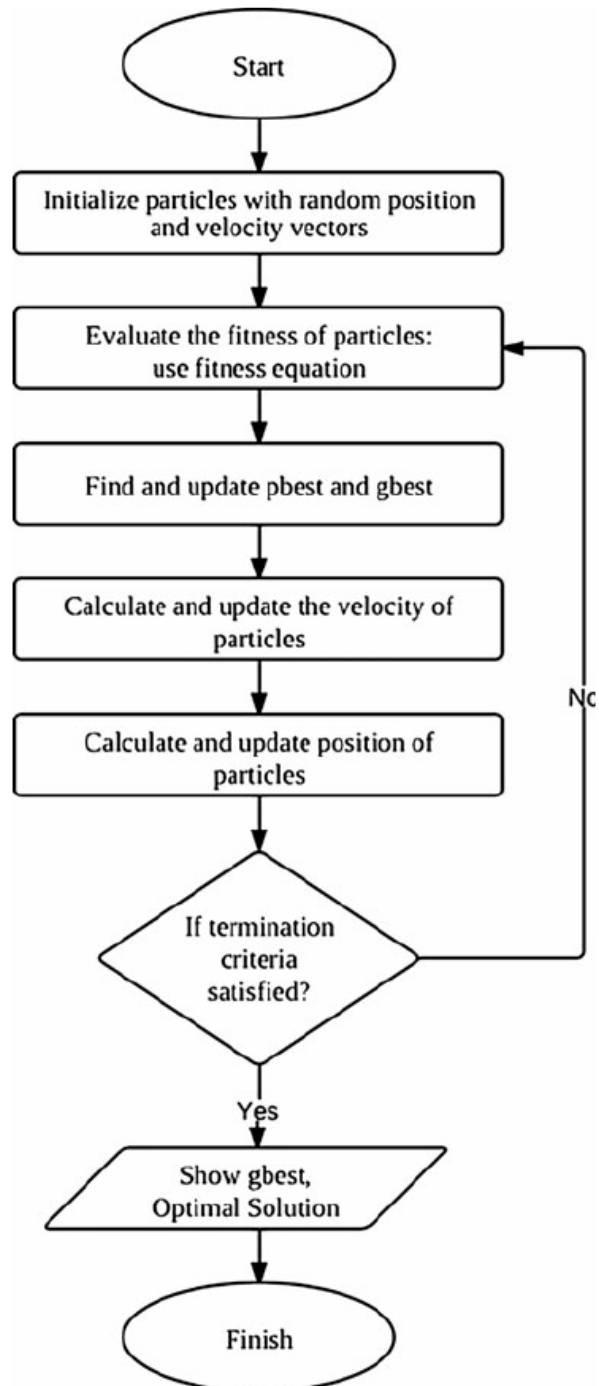
$$V(pj)^{t+1} = w.V(pj)^t + c_1.r_t.(pbest(jp) - X(pj)^t) + c_2.q^t.(gbest(j) - X(jp)^t) \quad \text{Eq. (6.1)}$$

and

$$X(jp)^{t+1} = X(jp)^t + V(jp)^{t+1} \quad \text{Eq. (6.2)}$$

Where,  $w$  is the inertia weight constant, which is a positive constant value. The parameter  $w$  is crucial for balancing the global search (for higher values of  $w$ ) known as *exploration*. The

parameter  $c_1$  and  $c_2$  are also positive constants known as *individual cognition parameter* and *social learning parameter* respectively, that weights the particle's own previous experience and the importance of the global learning of the swarm (Almeida and Leite, 2019). Parameters  $r$  and  $q$  also play the same role as  $c_1$  and  $c_2$ . The full flowchart of the algorithm (Armaghani et. al., 2013) is shown below.



Hybrid method comprising of both heuristic and deterministic methods are also often employed to take advantage of both the approaches. The heuristic method locates the region most likely for the global minimum. Once this is achieved the Hybrid search algorithm switches to the deterministic method to converge at the global minimum (Almeida and Leite, 2019). The particle swarm optimisation is a global optimisation scheme that searches the whole solution space for the minimum of all minima i.e., global minimum.

The MAGFORWARD program was first used to generate synthetic models and in the next step observed/real time data are utilised for the inversion code PSO2D code written independently, using Python programming language. In the beginning the program was developed for single body modeling for quick appraisal of the code.

Further, the MAGFORWARD and PSO2D program modified to accommodate the multiple bodies. Following results presented in Figures 6.2 and 6.3 along with results in Tables 6.1 and 6.2 shows the synthetic examples being tested with the particle swarm optimisation inversion scheme (Abdelrahman et al. 2015; Essa and Elhussein, 2018) with amplitude coefficient (K), Depth, Index angle, Structural Index (S.I) and location of the body ( $X_0$ ).

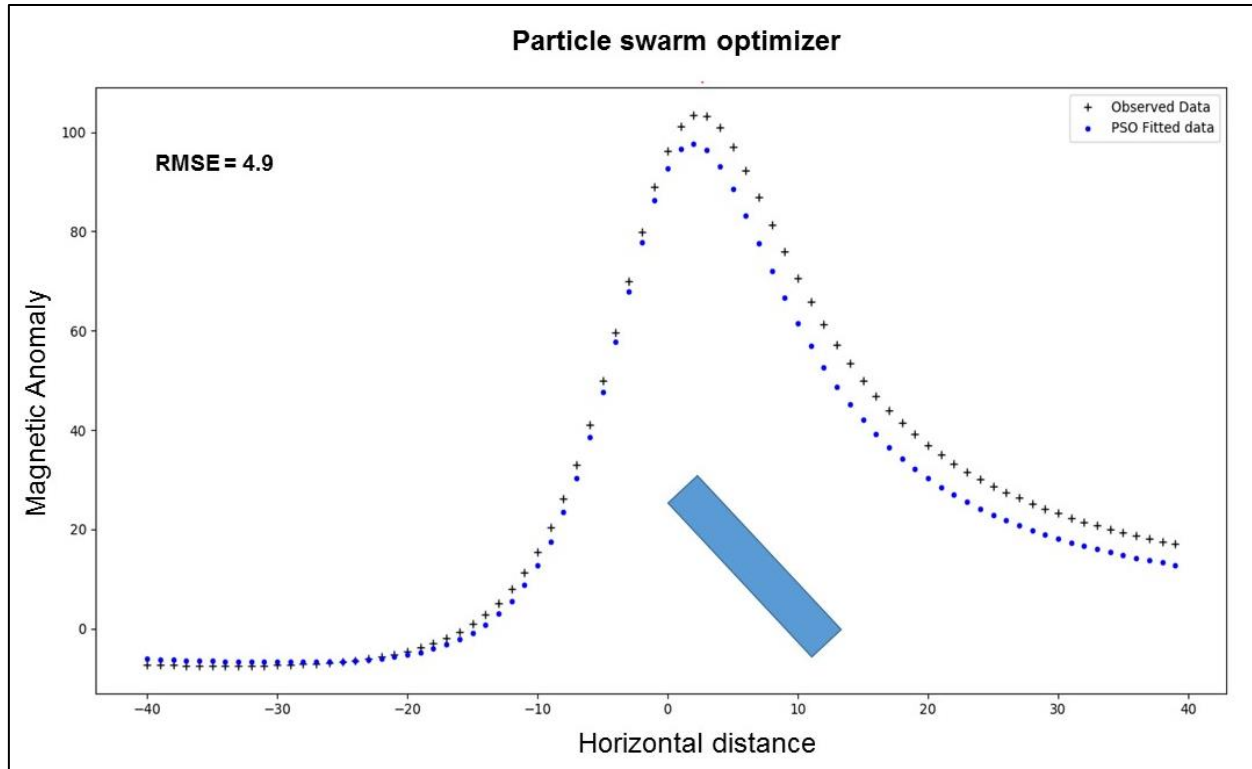


Figure 6.2. Forward modeling and PSO inversion of a thin sheet like geologic body. (Noise free). Black dots and blue dots show the observed and estimated data respectively.

Table-6.1. Observed and computed model parameters using PSO algorithm corresponding to figure-6.2.

Observed	Calculated
K = 1000 nT	K = 1331.53 nT
Depth = 9 m	Depth = 10.49 m
Index Angle = $-30^{\circ}$	Index Angle = $-32.3^{\circ}$
S.I = 1.0	S.I = 1.04
$X_0 = 0$	$X_0 = -0.85$

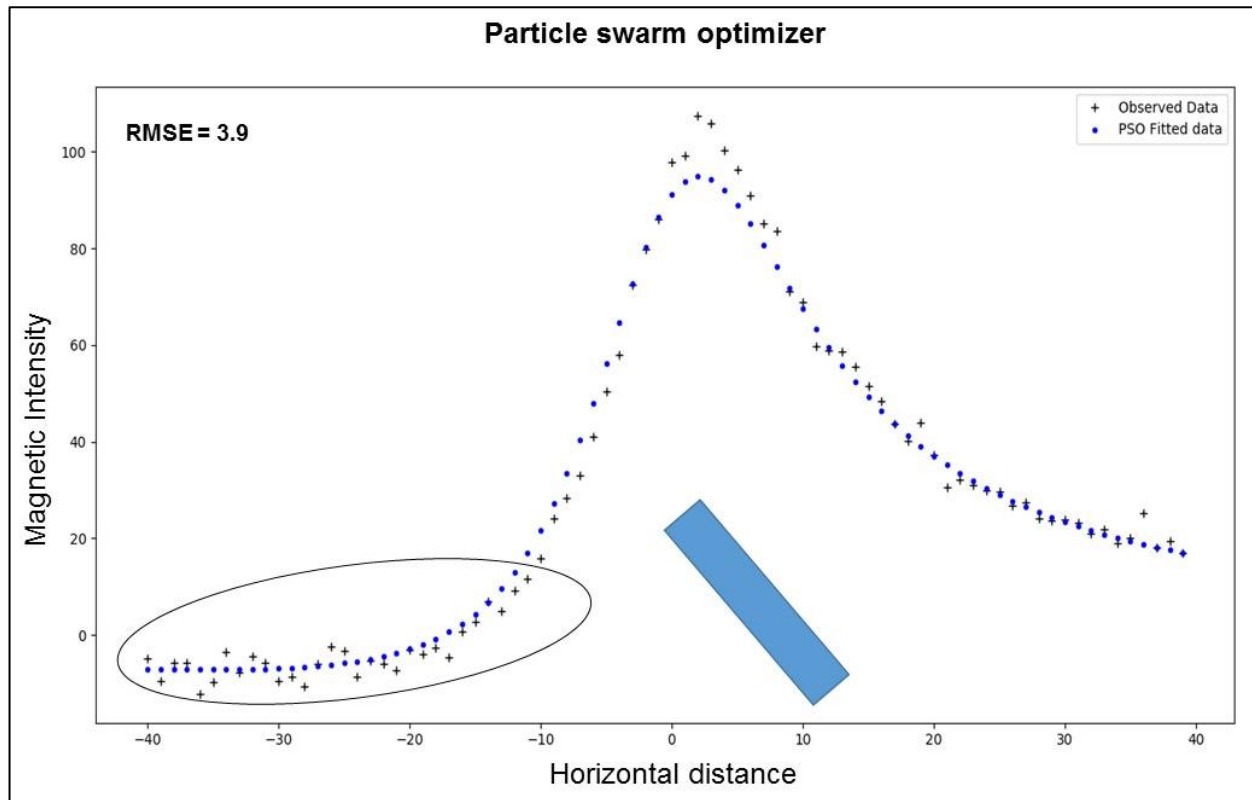


Figure 6.3. Forward modeling and PSO inversion of a thin sheet like geologic body. (with 5% gaussian noise, circled part). Black dots and blue dots show the observed and estimated data respectively. Horizontal distance in meter (m) and magnetic anomaly in nT.

Table 6.2. Observed and computed model parameters using PSO algorithm corresponding to figure 6.3.

Observed	Calculated
$K = 1000 \text{ nT}$	$K = 1439 \text{ nT}$
Depth = 9 m	Depth = 9 m
Index Angle = $-30^{\circ}$	Index Angle = $-32.7^{\circ}$
S.I = 1.0	S.I = 1.09
$X_0 = 0$	$X_0 = -0.49$

The above figures show the observed and computed model parameters for synthetic model comprising of single source anomaly. In Figure 6.2, 5% gaussian noise was added to check the efficacy of the algorithm towards random or uncorrelated noise. From the RMSE it is hence concluded that the method is quite robust to random noise levels too. Figure 6.4 shows the extension of the same exercise for multiple bodies shown in (Essa and Elhussein, 2018).

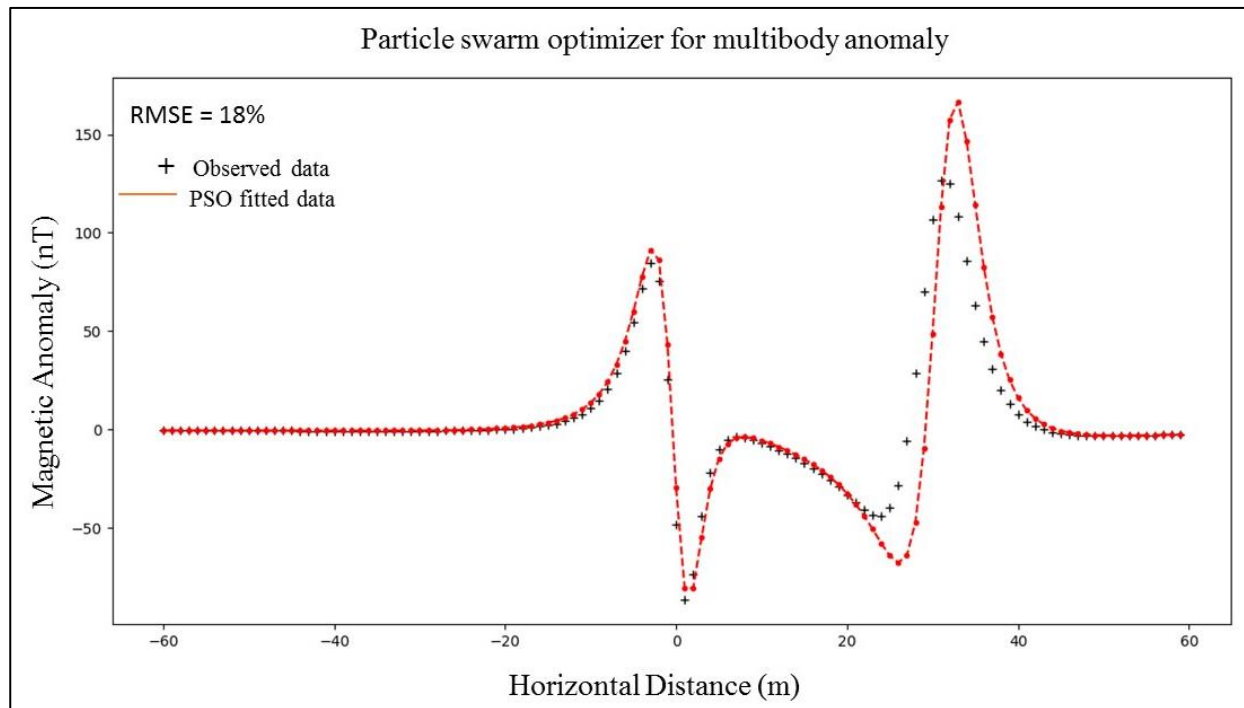


Figure 6.4. Forward modeling and PSO inversion of multibody anomaly (sphere and horizontal cylinder). (Noise free). Black 'plus' and red line show the observed and estimated data respectively.

## **CHAPTER-7**

### **MODELING AND INVERSION**

#### **7.1 2D Forward modeling of Magnetic data**

Forward modeling refers to the manual iterative method of modeling in which the model is modified to match the observed data. Forward modeling was done for the magnetic data along a profile to generate a subsurface geological model from the data and aid in the interpretation. The geologic model thus generated is useful in developing a better understanding about the causative sources and the subsurface geology.

The forward modeling was done in GMSYS module of Geosoft software, Oasis Montaj. The profile from the total magnetic intensity anomaly map was so chosen such that the profile covers maximum anticipated sources and geologic structures in the area as interpreted from the TMI map.

The model was refined until minimum rms was attained. Figure-7.1 shows the 2D forward modeling of magnetic data along a profile AB from Rajpura area, NE of Prithivipura, Sikar district, Rajasthan. Though the algorithm of the GMSYS module is capable of fitting polygonal type of bodies, the initial model was chosen so as to fit the observed and the computed data with tabular bodies (simple geometric body) and depth estimates from the Euler depth solutions were considered in modeling. This was intended to so as to have a comparison between the results of 2D forward modeling using commercial software and the developed PSO2D program.

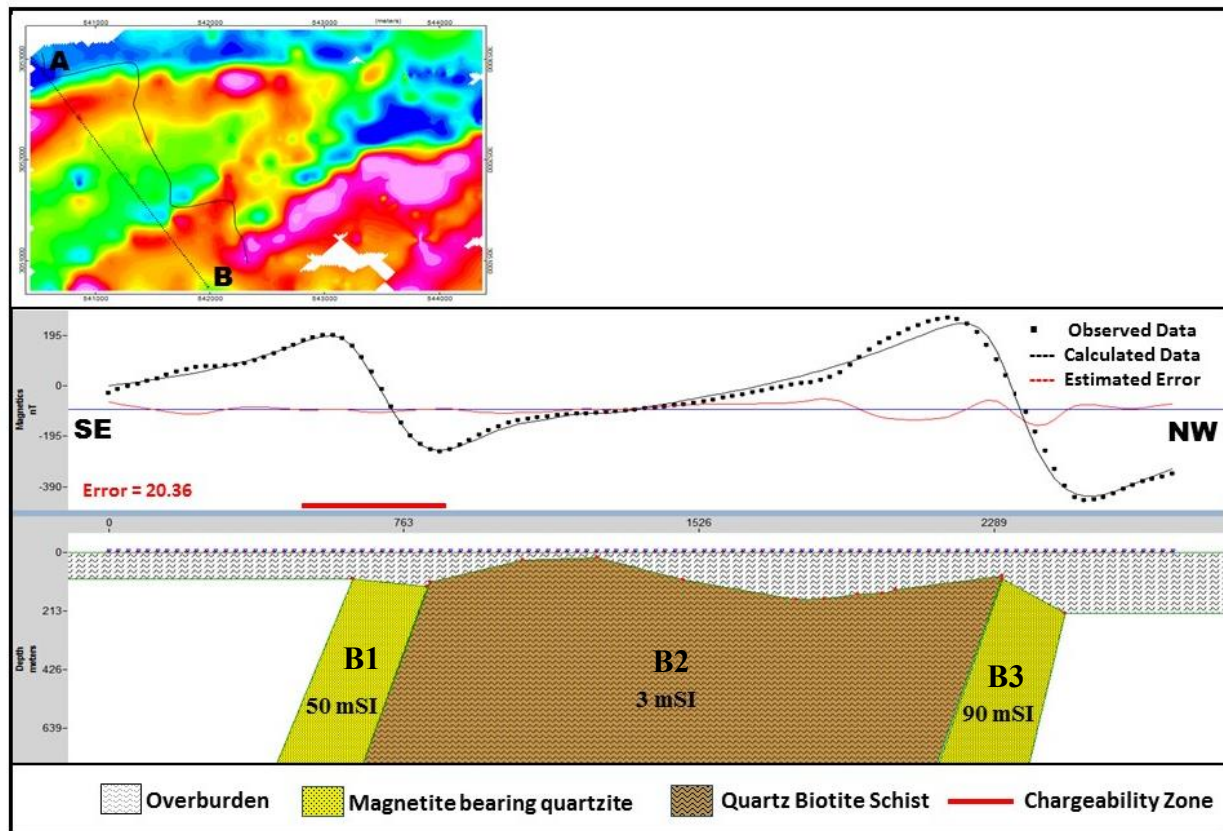


Figure 7.1. 2D forward model of magnetic data along profile AB from Rajpura area, NE of Prithivipura, Sikar district, Rajasthan.

One profile across the fold limb was taken and subjected to modeling in ModelVision 2.0 software. Different software has different algorithms to compute the forward magnetic response of bodies. Figure-7.2 shows 2D model of profile PQ generated in ModelVision 2.0 software and Table-7.1 shows the estimated parameters. The causative source parameters were estimated from the same. This data was later used to compare the results of the PSO2D program.

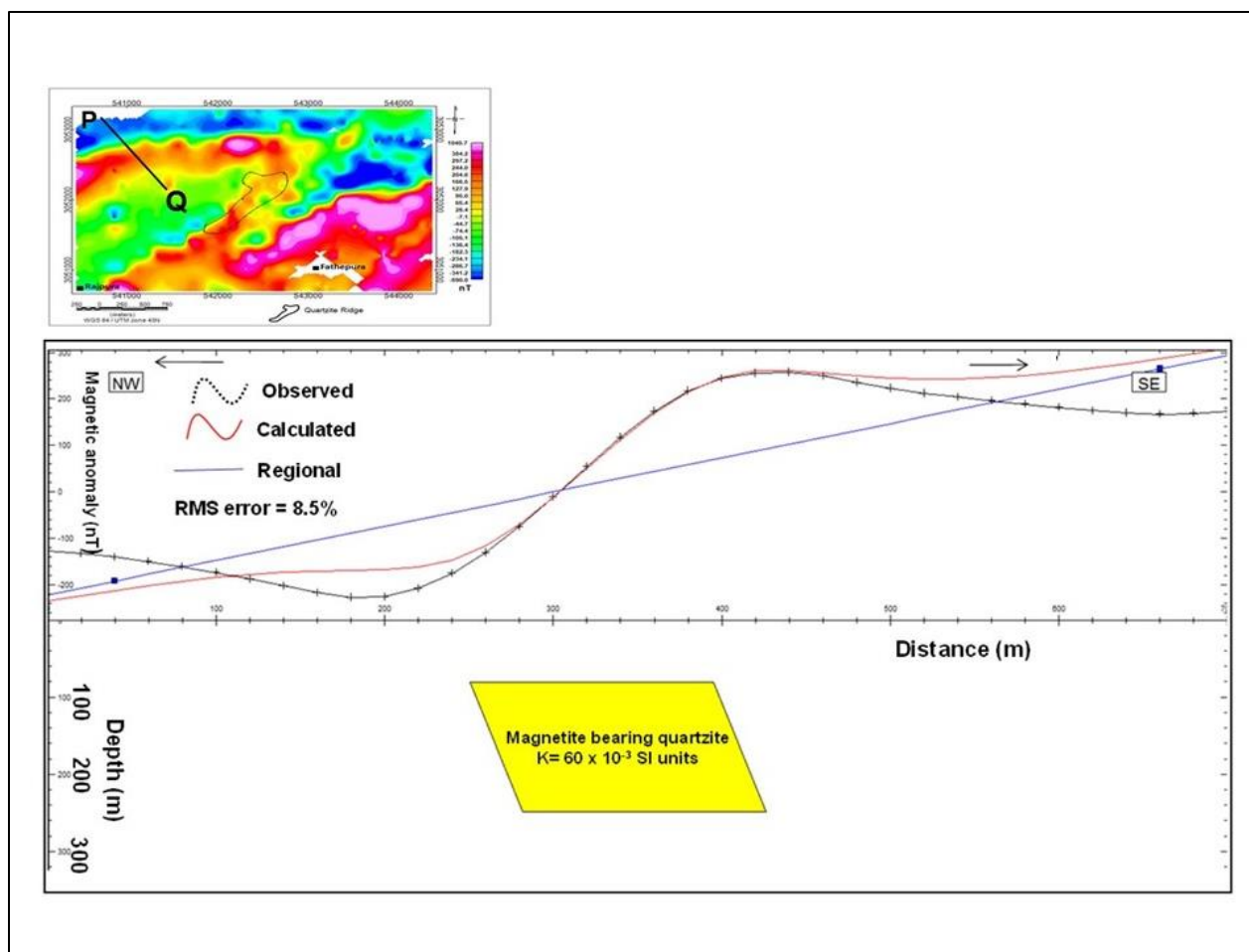


Figure 7.2. 2D forward model of magnetic data along profile PQ from Rajpura area, NE of Prithivipura, Sikar district, Rajasthan.

Table 7.1. Estimated parameters of the fold limb across profile PQ.

Profile Name	Body type	Depth to the top of the body (m)	Dip	Thickness (m)	Magnetic susceptibility $K \times 10^{-3}$ SI units
PQ (North western limb)	Tabular (Magnetite bearing quartzite)	118	$75^{\circ}$ SE	300	60

## 7.2 Particle Swarm Optimisation of magnetic data

Initially three profiles for chosen from the magnetic data across the northern limb of the fold in order to establish the dip direction, dip amount and depth to the top. These data were subjected to inversion using the particle swarm optimisation algorithm. The following figures show the inversion results.

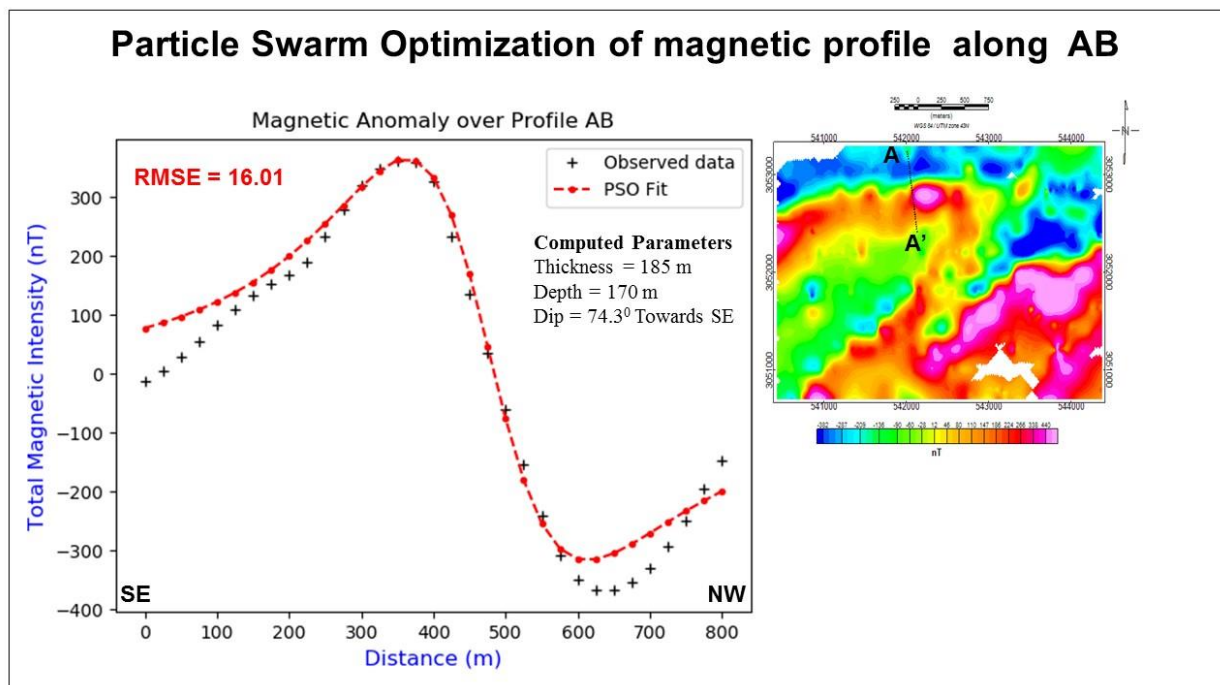


Figure 7.3. 2D PSO inversion of magnetic data along profile AA' from Rajpura area, NE of Prithivipura, Sikar district, Rajasthan.

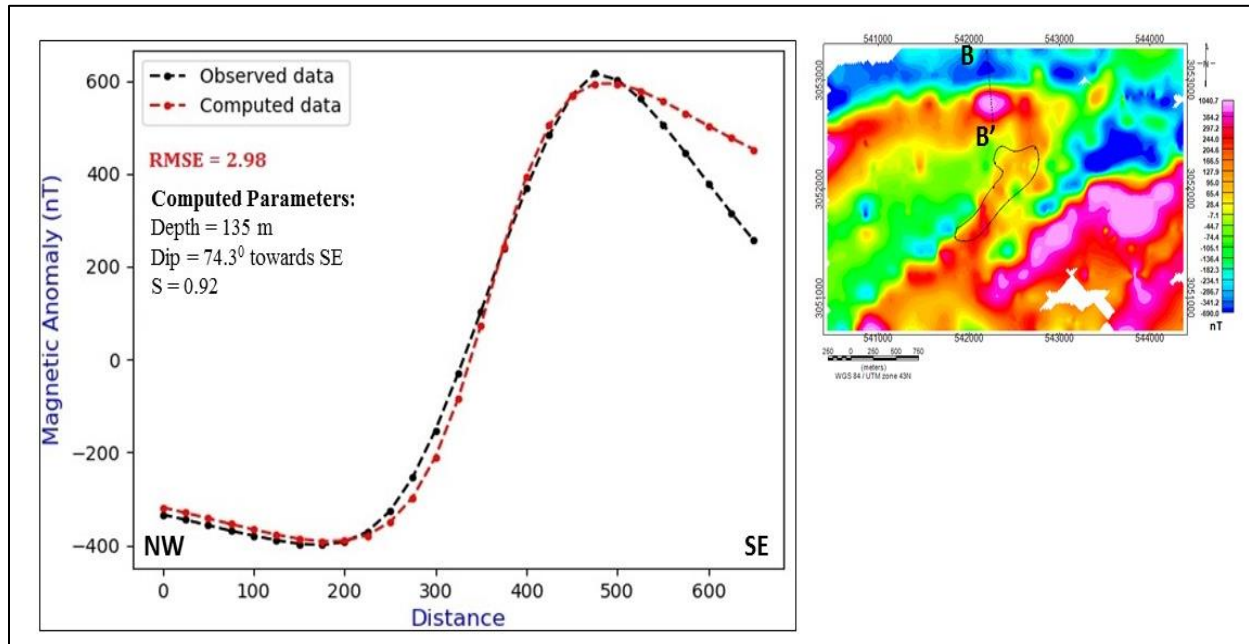


Figure 7.4. 2D PSO inversion of magnetic data along profile BB' from Rajpura area, NE of Prithivipura, Sikar district, Rajasthan.

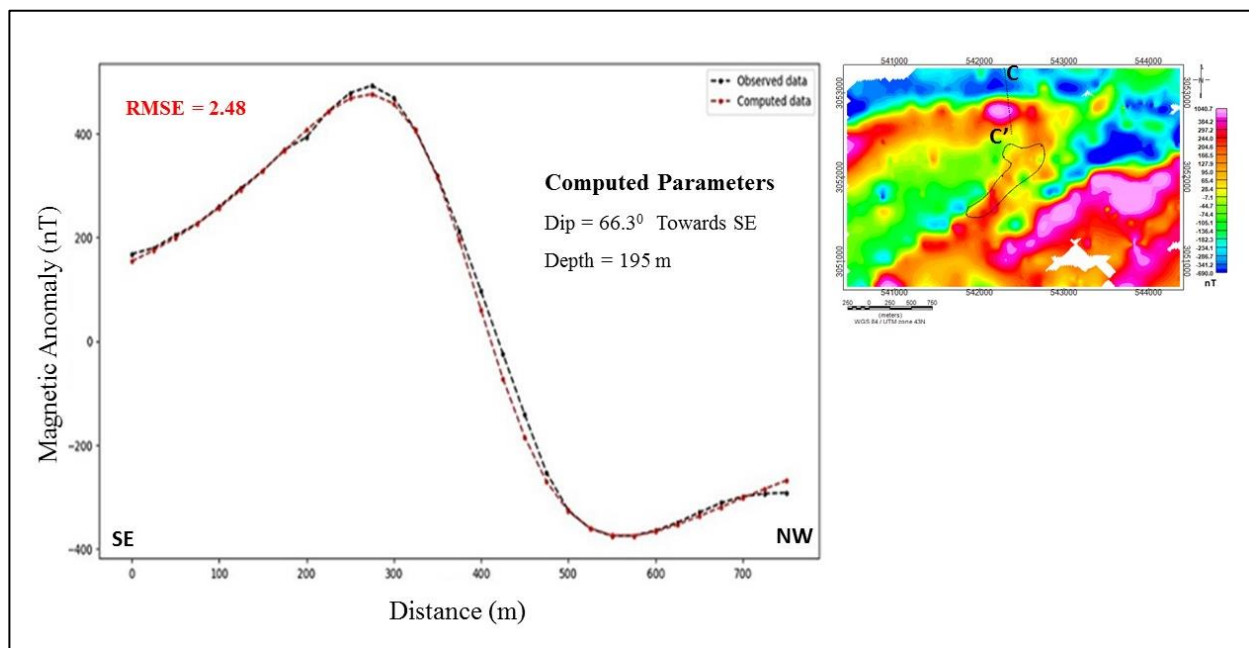


Figure 7.5. 2D PSO inversion of magnetic data along profile CC' from Rajpura area, NE of Prithivipura, Sikar district, Rajasthan.

Figure-7.3, 7.4 and 7.5 shows a good match between the observed and computed data. Profile BB' was taken in opposite direction to that of profile AA' and CC' to check whether the algorithm is capable of inversion irrespective of the direction of extracted profile. The initial parameter range fed to the program for all the three profiles are tabulated in Table-7.2.

Table 7.2. Used ranges for the inputs for PSO inversion of Profiles AA', BB' and CC'.

Parameter	Used range
K (Amplitude Coefficient)	0 – 60,000 nT
Theta ( $\theta$ )	-90 ⁰ to +90 ⁰
$X_0$ (Spatial location)	0 – 500 m
Z (Depth)	50 – 300 m
S (Structural index)	0 -2

The structural index for all the three profiles was found to be very close 1.0, which suggests that the type of body is sheet like. Geologically the limb of a fold can be best approximated by sheet like geometry.

The profile AB which was subjected to 2D forward modeling (Figure-7.1) in GMSYS module of Geosoft software, Oasis Montaj was subjected to particle swarm optimisation inversion algorithm. The inversion was carried out first with 100 iterations and 15 particles, gradually with each run the optimum solution was found for 500 iterations and 50 particles. As the developed PSO2D program can't model polygonal bodies in contrast to the GMSYS modeling, an exact match between the computed and observed anomaly is not obtained. Figure-

7.6 shows the PSO inversion of profile AB from the TMI map of the study area and the swarm parameters used in the inversion of profile AB are tabulated in Table-7.3.

Table 7.3. Swarm parameters used in the inversion of magnetic data.

Swarm Parameter	Value used
Particle Inertia	0.01
Local weight	1.2
Global weight	1.5
Maximum velocity	1.0
Step length	0.05

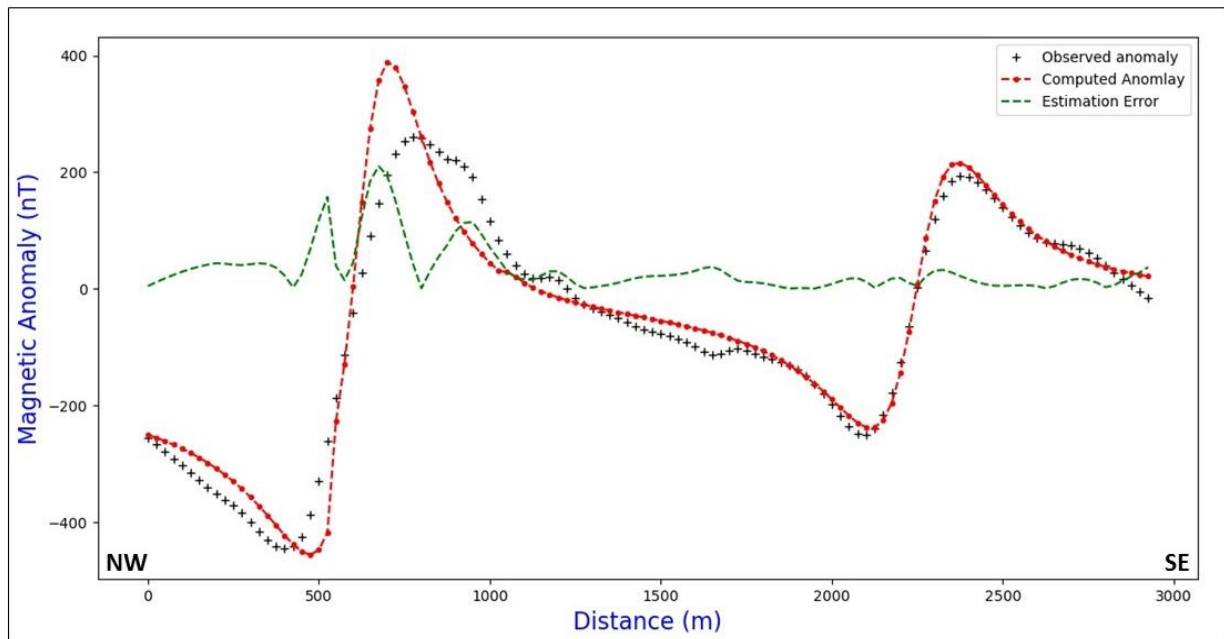


Figure 7.6. PSO inversion of magnetic data across profile AB. (Black line: Observed anomaly, Red line: Computed anomaly, Green line: Estimation error).

Magnetic data modeling using polygonal geometry is computationally cumbersome also computation time is longer. Proper choice of regular geometric bodies can also solve the purpose

with estimation error in the acceptable range. The inversion results along with comparison of results with that of GMSYS modeling is tabulated in Table-7.4.

Table 7.4. Inversion results and comparison with the GMSYS modeling, ModelVision modeling and Euler Depth.

S. no.	Lithology	Depth (PSO)	Dip (PSO)	Depth (GMSYS)	Depth (Euler)	Depth (Model Vision)	% Error
B1	Magnetite bearing quartzite	150m	68 ⁰	120m	120-150m	-	<b>PSO: 22.18</b>
B2	Quartz biotite schist	170m	67.7 ⁰	160m	-	-	<b>GMSYS: 20.36</b>
B3	Magnetite bearing quartzite	170m	75 ⁰	150m	150-180m	120m	<b>ModelVision: 8.5</b>

### 7.2.1 Inference about Particle Swarm optimisation algorithm

The modeling attempted in commercial softwares as well as the developed PSO2D program has good match and comparable results. All the approaches suggest that the fold limbs are SE dipping with a dip amount ranging from 65⁰ to 75⁰. The depth ranges from 120 m to 200 m. The depth estimated using the algorithm is higher than the GM-SYS model, this is an ambiguity as a number of combinations of susceptibility, thickness and depth can return identical anomalies.

## 7.3 Integrated interpretation

Integrated interpretation refers to the process of interpretation and arriving at an inference taking into account of all the processed data sets and models. The integrated interpretation was made taking the magnetic and IP/Resistivity data and models. From these data it is observed that

the high chargeability zones are correlated with moderate to high magnetic anomalies and resistivity gradients signifying the sheared contact. The chargeability is seen to be at the gradient of magnetic anomaly map which can be inferred as the presence of disseminated sulphides along the weak planes in quartz biotite schist and the sheared contact between the magnetite bearing quartzite and the quartz biotite schist. Figure 7.7 shows the chargeability contours (High) superimposed over the reduced to pole magnetic map.

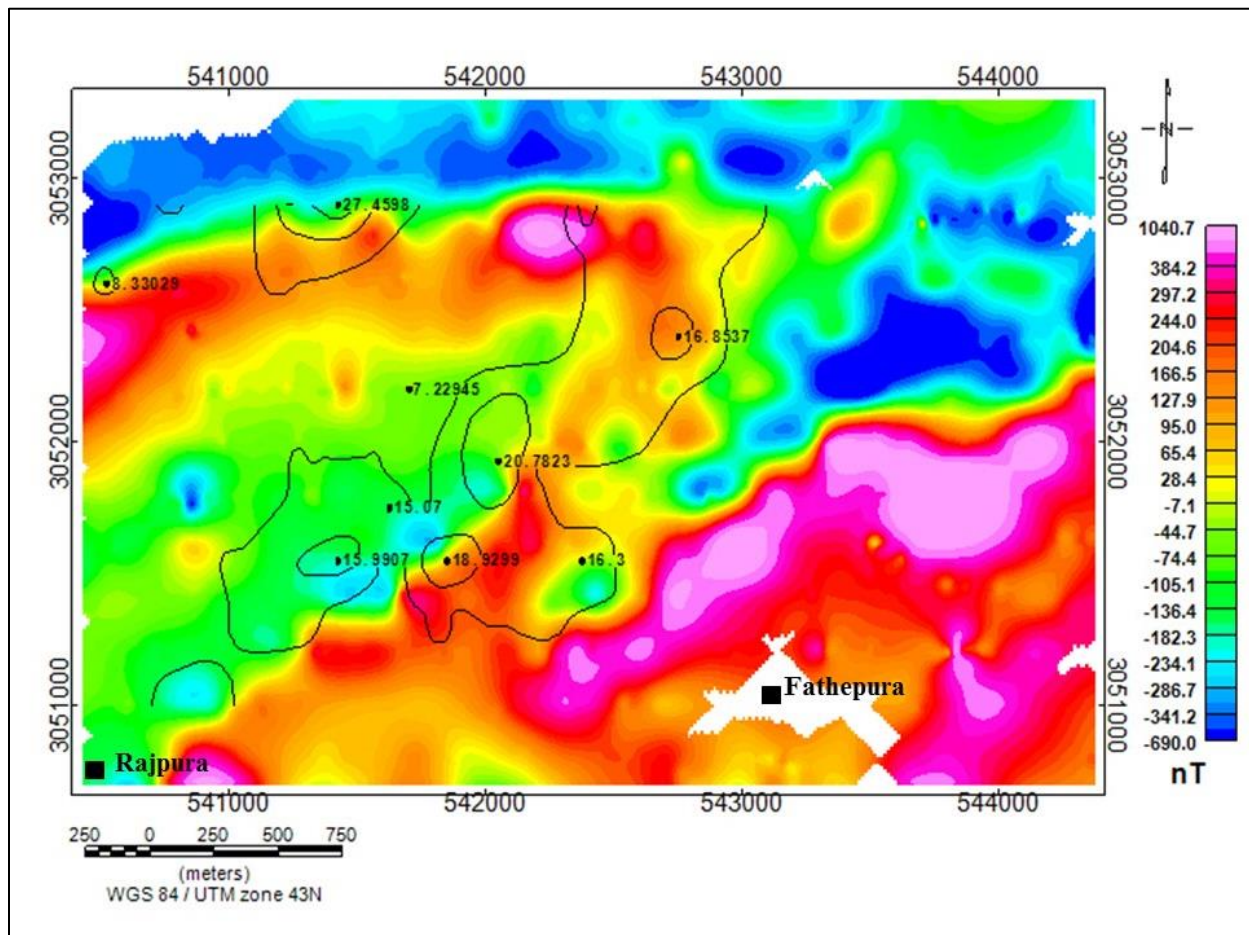


Figure 7.7. High chargeability contours superimposed over the reduced to pole (RTP) magnetic map.

## **CHAPTER – 8**

### **RESULTS AND CONCLUSIONS**

- Magnetic data revealed a high magnetic folded structure in the area. The magnetic high is attributed to magnetite bearing quartzite and the low is attributed to quartz biotite schist.
- IP/Resistivity data delineated three significant high chargeability zones trending in NE-SW direction with a width of ~300 m over a strike length of 2.5-3 km.
- Modeling of the magnetic data (TMI data) indicated that both the limbs of the folded structure are dipping in SE direction and it is indicating the fold to be overturned.
- The results of the developed Particle Swarm optimisation inversion were found to be in an agreement with the modeling done using commercial software for simple structure, sheet like bodies. And the depth estimated from Euler Deconvolution method and the algorithm are also found to be in good correlation.
- The model parameter dimensionality handling and rate of convergence of the algorithm is found to be much higher than forward modeling methods for bodies of simple geometry.
- The depth to the top of the causative magnetic sources were estimated in the range of 120 to 200 m from combined estimates using commercial software and PSO2D algorithm.

- High chargeability is observed to fall at the gradient of the high magnetic anomalies. The chargeability is due to the disseminated sulphides. The spatial distribution of the chargeability zones suggests that the dissemination of sulphides is in the weak planes in quartz biotite schist or the sheared contact between magnetite bearing quartzite and quartz biotite schist.
- The correlation of the resistivity and IP data reveals that the high chargeability is associated with low to moderate resistivity values in the area attributed to quartz-biotite-schist/sheared QBS.
- Magnetic data inferred the nature of fold and their spatial disposition. High chargeability is due to disseminated sulphides along the sheared/fractured contact between QBS and quartzites indicating the potential target areas for uranium mineralization.

**Future scope of work:**

In the present study the global optimisation approach namely, Particle Swarm Optimisation algorithm was independently developed in Python and used for the inversion and modeling of magnetic data, acquired during the course of the study. The PSO algorithm has been found fast, efficient and easy to implement for the modeling of geophysical data. For the future scope of this work the same PSO algorithm can be extended and applied for the inversion of IP/Resistivity data. PSO algorithm has been used in inversion of IP/Resistivity data previously by some workers (Shaw and Shalivahan, 2007) for sounding data, but the implementation has not yet been done in the inversion of gradient IP/Resistivity data. By analysing and formulating the forward problem, inversion for the gradient IP/Resistivity data can also be carried out using PSO method.

## References:

- Abdelrahman, E. M., and Essa, K. S., (2015). A new method for depth and shape determination from magnetic data. *Pure Appl. Geophys.*, v.172. pp.439-460.
- Al-Garni, M.A., (2016). Artificial neural network inversion of magnetic anomalies caused by 2D fault structures. *Arab J Geosci*, v.9, pp.156.
- Almeida, B.S.G. and Leite, V. C., (2019). Particle Swarm Optimisation: A Powerful Technique for Solving Engineering Problems, *Swarm Intelligence - Recent Advances, New Perspectives and Applications*, Javier Del Ser, Esther Villar and Eneko Osaba, IntechOpen, DOI: 10.5772/intechopen.89633. Available from: <https://www.intechopen.com/books/swarm-intelligence-recent-advances-new-perspectives-and-applications/particle-swarm-optimisation-a-powerful-technique-for-solving-engineering-problems> .
- Armaghani, J., Danial, Mohsen, H., Edy, T., Aminaton, M., and Ahmad, N. S., (2013). Blasting-Induced Flyrock and Ground Vibration Prediction through Expert Artificial Neural Network Based on Particle Swarm Optimisation. *Arabian Journal of Geosciences*. DOI: 10.1007/s12517-013-1174-0.
- Banerjee, D. M., Basu, P. C., & Srivastava, N. (1980). Petrology, mineralogy, geochemistry, and origin of the Precambrian Aravallian phosphorite deposits of Udaipur and Jhabua, India. *Economic Geology*, v.75(8), pp.1181-1199.
- Baranov, V., and Naudy H. (1964). Numerical calculation of the formula of reduction to the magnetic pole. *Geophysics*, v.29, pp.67–79.
- Bhattacharya, B.B., Shalivahan (2016). *Geo-electric Methods theory and applications*. McGraw Hill education, India, pp.433-518.

- Biswas, A. and Acharya, T., (2016). A very fast simulated annealing method for inversion of magnetic anomaly over semi-infinite vertical rod-type structure. *Modeling earth system and environment*, v.2, pp.1-10.
- Blakely, R. J., (1995). *Potential theory in gravity and magnetic applications*: Cambridge University Press, United Kingdom.
- Das A.R., (1988). Geometry of the superposed deformation in the Delhi Supergroup of rocks, north of Jaipur, Rajasthan. In: A.B. Roy (ed), *Precambrian of the Aravalli Mountain, Rajasthan, India*. Geological Society of India. v.7, pp.247-266.
- Dasgupta, S. P. (1968). The structural history of the Khetri Copper Belt, Jhunjhunu and Sikar districts, Rajasthan. *Mem. Geological Survey of India*, pp.98-168.
- Dar, K. K. (1964). Some geological data on atomic energy minerals in India. *Geological Society of India*, v.5, pp.111-120.
- Dentith, M (2003). Geophysical signatures of South Australian mineral deposits: Miscellaneous and minor deposits, ASEG Extended Abstracts, 2003:3, 257-281, DOI: 10.1071/ASEGSpec12_20.
- Dobrin, M.B. & Savit, C.H. (1988). *Introduction to Geophysical Prospecting*. Fourth edition. McGraw Hill, New York. pp.
- Essa, K. S., and Elhussein, M., (2018). PSO (Particle Swarm Optimisation) for interpretation of magnetic anomalies caused by simple geometrical structures: *Pure Appl. Geophys*, v.175, pp.3539-3553.

- Finn, C. A., ed., (2002). Examples of the utility of magnetic anomaly data for geologic mapping. U. S. Geological Survey Open-file Report 02-0400, available at <http://pubs.usgs.gov/of/2002/ofr-02-0400/>.
- Gangopadhyay, P. K., & Sen, R. (1972). Trend of regional metamorphism: an example from “Delhi System” of rocks occurring around Bairawas, north-eastern Rajasthan, India. *Geologische Rundschau*, v.61(1), pp.270-281.
- Heron, A. M., (1953). The geology of central Rajputana. *Memoir Geological Survey of India*, v.79, pp.1-389.
- Hinze, W.J., Frese, R.R.B., Saad, A.H., (2013). *Gravity and Magnetic Exploration: Principles, Practice, and Applications*. Cambridge University Press, pp.180-195.
- Hohmann, G. W., & Ward, S. H. (1981). Electrical methods in mining geophysics: *Econ. Geol.*, v.75, pp.806-828.
- Hubbard, S. S. and Linde, H., (2011). *Hydrogeophysics. Treatise on Water Science*. pp.401-434.
- INTERNATIONAL ATOMIC ENERGY AGENCY, (2015). *World Distribution of Uranium Deposits (UDEPO) with Uranium Deposit Classification*. pp.06-08.
- Kennedy, J., & Eberhart, R. (1995). Particle swarm optimisation: In *Proceedings of ICNN'95-International Conference on Neural Networks*. v. 4, pp. 1942-1948. IEEE.
- Kearey Philip, Michael Brooks and Ian Hill. (2002). *An Introduction to Geophysical Exploration* Third Edition. Osney Mead, Oxford, Blackwell Science Ltd. pp.
- Keating, P., (1995). A simple technique to identify magnetic anomalies due to kimberlite pipes. *Exploration and Mining geology*, v.4(2), pp.121-125.

- Kramer, O., Claurri, D.E. and Koziel, S., (2011). Derivative-Free Optimisation, Computational Optimisation, Methods and Algorithms. pp.61-83. DOI: 10.1007/978-3-642-20859-1_4.
- Kumar, I., Kumar, B. V., Babu, R. V., Dash, J. K., & Chaturvedi, A. K., (2019). Relaxation time distribution approach of mineral discrimination from time domain-induced polarisation data. *Exploration Geophysics*, v.50(4), pp.337-350.
- Langel, R. A. and Estes, R. H. (1982). A Geomagnetic Field Spectrum: Geophysical Research Letters, v.9, no.4, pp.250-253.
- Lee, K. Y., & Park, J. B., (2006). Application of particle swarm optimization to economic dispatch problem: advantages and disadvantages. In 2006 IEEE PES Power Systems Conference and Exposition, pp. 188-192.
- Loke, M. H. (2004). Tutorial: 2-D and 3-D electrical imaging surveys.
- Lowes, F. J., (1974). Spatial power spectrum of the main geomagnetic field, and extrapolation to the core. *Geophysical Journal International*, v.36. pp.717-730.
- Macnae, J. C., (1979). Kimberlites and exploration geophysics: *Geophysics*, v.44, pp.1395-1416.
- Marshall, D. J., & Madden, T. R. (1959). Induced polarization, a study of its causes. *Geophysics*, v.24(4), 790-816.
- Martínez, J., Rey, J., Sandoval, S., Hidalgo, M., & Mendoza, R. (2019). Geophysical prospecting using ERT and IP techniques to locate Galena veins. *Remote Sensing*, v.11(24), p.2923.
- Mauersberger, P., (1956). The mean of the energy density of the main geomagnetic field on the earth's surface and its solar change. *Gerlands Beitr. Geophys*, v.65, pp.207-215.

- Menke, W., (1984). Geophysical data analysis: Discrete inverse theory: International Geophysics Series, Academic Press Inc., v.45, pp.289.
- Miguel, B.,(2007). Monte Carlo Inversion of Gravity and Magnetic Data in 3D. AGU Spring Meeting Abstracts.
- Mishra, D. and Shalivahan, (2015). Sensitivity plots using comsol 5.1 multi physics; a tool for optimizing geophysical field survey. In Proceedings of 2015 COMSOL Conference.
- Nabighian, M. N., Grauch, V. J. S., Hansen, R. O. and Lafehr, T. R. (2005). The historical development of the magnetic method in exploration. *Geophysics*, v.70, no.6, pp.33-61.
- Naha, K., Mukhopadhyay, D. K., and Mohanty, R., (1988). Structural evolution of the rocks of the Delhi group around Khetri, north eastern Rajasthan. *Geol. Soc. India-Mem. No.7*, pp.207-245.
- Pears, G. and Chalke, T., (2016). Geological and geophysical integrated interpretation and modelling techniques, ASEG Extended Abstracts, 2016:1, 1-7, DOI: 10.1071/ASEG2016ab262.
- Pelton, W. H., Ward, S. H., Hallof, P. G., Sill, W. R., and Nelson, P. H. (1978). Mineral discrimination and removal of inductive coupling with multifrequency IP: *Geophysics*, v.43(3), pp.588-609.
- Power, M., Belcourt, G., & Rockel, E. (2004). Geophysical methods for kimberlite exploration in northern Canada. *The Leading Edge*, v.23(11), pp.1124-1129.
- Rajaraman, H.S., Babu, V.R., Dandele, P.S., Chavan, S.J., Achar, K.K., and Babu, P.V.R. (2011). *The leading edge*. v.30(10), pp. 1158-1161.

- Ray, S. K. (1987). Albitite occurrences and associated ore minerals in the Khetri Copper Belt, north-eastern Rajasthan. *Rec. Geol. Surv. India*, v.113(7), pp.41-49.
- Reid, A. B., Allsop, J. M., Granser, H., Millett, A. J., and Somerton, I. W. (1990). Magnetic interpretation in three dimensions using Euler deconvolution. *Geophysics*, v.55, pp.80–91.
- Ross, G. M., J. Broome, and W. Miles., (1994). Potential fields and basement structure: Western Canada Sedimentary Basin, *in* G. D. Mossop and I. Shetsen, comps., *Geological atlas of the Western Canada Sedimentary Basin: Canadian Society of Petroleum Geologists and Alberta Research Council*, pp.41-46.
- Roux, A. T., (1970). The application of geophysics to gold exploration in South Africa, *in* L. W. Morley, ed., *Mining and ground water geophysics, 1967: Geological Survey of Canada, Economic Geology Report No. 26*, pp.425-438.
- Sambridge, M. and Mosegaard, K., (2002). Monte Carlo methods in geophysical inverse problems. *Reviews of geophysics*. v.40(3). pp.1-29.
- Sharma, R.S., (1988). Patterns of metamorphism in the Precambrian rocks of the Aravali mountain belt. In: Roy A.B. (ed.) *Precambrian of the Aravali mountain, Rajasthan, India. Geological society of India Memoir*. v.7, pp.33-76.
- Shaw, R. and Srivastav, S., (2007). Particle Swarm Optimisation: A new tool to invert geophysical data. *Geophysics*, v.72(2), pp.75-83.
- Simpson, F., and Bahr, K., (2005). *Practical Magnetotellurics*, Cambridge University Press, United Kingdom.

- Singh, S. P., (1988). Stratigraphy and sedimentation pattern in the Proterozoic Delhi Super Group, north western India. In: A. B. Roy (Eds.) Precambrians of Aravalli Mountain, Rajasthan, India. Memoir Geological Society of India. pp.193-205.
- Sinha-Roy, S., Malhotra, G. And Mohanty, M., (1998). Geology of Rajasthan, Geological Society of India, pp.127-152.
- Srinivasa Rao, B., Subash Ram., Roshan Ali Shaik., Vinay Kumar., Dash, J.K., Purohit, R.K and Chaturvedi, A.K., (2016). Applications of integrated Geophysical Techniques to Delineate Favourable Structures and Conductive Zones for Uranium Mineralisation in Narsinghpuri-Salwari areas, Sikar District, Rajasthan. Journal of Geophysics, pp.191-196.
- Srivastava, S., Datta, D., Agarwal, B.N.P. and Mehta, S., (2013). Applications of Ant colony optimisation in determination of source parameters from total gradient of potential fields. Near surface geophysics, v.12-3, pp.373-390.
- Sumner, J.S., (1976). Principles of induced polarization for geophysical exploration. Elsevier scientific publishing company. Netherlands. v.5, pp.1-277.
- Sundararajan, N., Pracejus, B., Al-Khirbash, S., Al-Hosni, T. K., Ebrahimi, A., and Al-Mushani, M., (2017). Magnetic mapping for delineating structures favorable to uranium mineralization in Dhofar region, Sultanate of Oman. Int J Earth Environ Sci, v.1, p.127.
- Tarantola, A., (2005). Inverse problem theory and methods for model parameter estimation. Society of industrial and applied mathematics, Philadelphia.
- Telford, W. M., Telford, W. M., Geldart, L. P., Sheriff, R. E., and Sheriff, R. E. (1990). Applied geophysics. Cambridge university press.

- Van Voorhis, G. D., Nelson, P. H., & Drake, T. L., (1973). Complex resistivity spectra of porphyry copper mineralization. *Geophysics*, v.38(1), pp.49-60.
- Yadav, O. P., Hamilton, S., Vimal, R., Saxena, S. K., Pande, A. K., and Gupta, K. R. (2002). Metasomatite-albitite-hosted uranium mineralisation in Rajasthan. *Exploration and Research for Atomic Minerals*, v.14, pp.109-130.
- Yadav, G. S., & Singh, S. K. (2007). Integrated resistivity surveys for delineation of fractures for ground water exploration in hard rock areas. *Journal of applied geophysics*. v.62(3), pp. 301-312.